Solar Phys (2014) 289:4173–4208
DOI 10.1007/s11207-014-0571-1

An Ensemble Study of a January 2010 Coronal Mass Ejection (CME): Connecting a Non-obvious Solar Source with Its ICME/Magnetic Cloud

D.F. Webb · M.M. Bisi · C.A. de Koning · C.J. Farrugia · B.V. Jackson · L.K. Jian · N. Lugaz · K. Marubashi · C. Möstl · E.P. Romashets · B.E. Wood · H.-S. Yu

Received: 11 March 2014 / Accepted: 30 June 2014 / Published online: 31 July 2014

Abstract A distinct magnetic cloud (MC) was observed *in-situ* at the *Solar TErrestrial RElations Observatory* (STEREO)-B on 20 – 21 January 2010. About three days earlier, on 17 January, a bright flare and coronal mass ejection (CME) were clearly observed by STEREO-B, which suggests that this was the progenitor of the MC. However, the *in-situ*

Electronic supplementary material The online version of this article (doi:10.1007/s11207-014-0571-1) contains supplementary material, which is available to authorized users.

D.F. Webb (✉)
ISR, Boston College, Chestnut Hill, MA, USA
e-mail: david.webb@bc.edu

M.M. Bisi
RAL Space Science & Technology Facilities Council, Rutherford Appleton Laboratory, Harwell Oxford, Oxfordshire, England, UK

C.A. de Koning
NOAA Space Weather Prediction Center and University of Colorado, CIRES, Boulder, CO, USA

C.J. Farrugia · N. Lugaz
Space Science Center & Department of Physics, University of New Hampshire, Durham, NH, USA

B.V. Jackson · H.-S. Yu
Center for Astrophysics and Space Science, University of California, San Diego, La Jolla, CA, USA

L.K. Jian
Heliophysics Science Division, Code 672, NASA Goddard Space Flight Center, Greenbelt, MD, USA

L.K. Jian
Department of Astronomy, University of Maryland, College Park, MD, USA

K. Marubashi
Korea Astronomy and Space Science Institute, Daejeon, Korea

Present address:
K. Marubashi
Sayama, Saitama 350-1317, Japan

speed of the event, several earlier weaker events, heliospheric imaging, and a longitude mismatch with the STEREO-B spacecraft made this interpretation unlikely. We searched for other possible solar eruptions that could have caused the MC and found a faint filament eruption and the associated CME on 14 – 15 January as the likely solar source event. We were able to confirm this source by using coronal imaging from the *Sun Earth Connection Coronal and Heliospheric Investigation* (SECCHI)/EUVI and COR and *Solar and Heliospheric Observatory* (SOHO)/*Large Angle and Spectrometric Coronograph* (LASCO) telescopes and heliospheric imaging from the *Solar Mass Ejection Imager* (SMEI) and the STEREO/*Heliospheric Imager* instruments. We use several empirical models to understand the three-dimensional geometry and propagation of the CME, analyze the *in-situ* characteristics of the associated ICME, and investigate the characteristics of the MC by comparing four independent flux-rope model fits with the launch observations and magnetic-field orientations. The geometry and orientations of the CME from the heliospheric-density reconstructions and the *in-situ* modeling are remarkably consistent. Lastly, this event demonstrates that a careful analysis of all aspects of the development and evolution of a CME is necessary to correctly identify the solar counterpart of an ICME/MC.

1. Introduction

Coronal mass ejections (CMEs) and their interplanetary counterparts (ICMEs) are large expulsions of plasma and magnetic flux from the solar corona into the heliosphere. Their interior magnetic fields are thought to form giant helical flux tubes, with radial scale sizes of tenths of an AU when they are observed *in-situ* by spacecraft. Such measurements of ICMEs and their magnetic structures have been largely restricted to single-point observations in space, resulting in too many free parameters to unambiguously determine their large-scale shape, geometry, and magnetic-field topology. From a space-weather point of view, researchers use the near-Sun and *in-situ* measurements in numerical simulations or empirical models to improve the prediction of the ICME shock and magnetic-ejecta arrival time at Earth. However, to fully understand the physical propagation and principal direction of a CME in the solar wind, we need three-dimensional (3D) reconstructions, based on heliospheric imaging, to permit us to "fill in" the temporal and spatial gaps between the near-Sun and *in-situ* data to provide a truly global view of the propagation and interactions of the CME plasma as it moved through the inner heliosphere.

In this article we analyze a fairly average CME launched amid varying solar activity, bringing to bear different sets of observations and 3D reconstructions and empirical models to understand the global geometry and propagation of the CME, to analyze its *in-situ* characteristics, and to investigate the characteristics of the MC by comparing flux-rope model

C. Möstl
Institute of Physics, University of Graz, 8010 Graz, Austria

C. Möstl
Space Research Institute, Austrian Academy of Sciences, 8042 Graz, Austria

E.P. Romashets
Lone Star College, 2700 West W. Thorne Drive, Houston, TX, USA

B.E. Wood
Space Science Division, Naval Research Laboratory, Washington, DC, USA

fits. As with several recent studies (*e.g.* Webb *et al.*, 2012), we find that heliospheric imaging observations must be included with solar observations and *in-situ* measurements to fully understand the global geometry and heliospheric propagation of CMEs.

On 17 January 2010, before rotating onto the Earth-facing disk and producing a series of M-class X-ray flares, Active Region 11041 was associated with an energetic CME with a coronal wave and dimming, and radio Type II and III emission. A magnetic cloud (MC) was observed at STEREO-B (ST-B) on 20 – 21 January, and the first impression from the views near the Sun from the *Solar TErrestrial RElations Observatory* (STEREO: Kaiser *et al.*, 2008), and *Solar and Heliospheric Observatory* (SOHO: Domingo, Fleck, and Poland, 1995) spacecraft was that at least part of the 17 January CME reached STEREO-B (ST-B), where the MC was observed. Further investigation, however, led us to identify an earlier CME erupting on 14 – 15 January that was likely aimed toward ST-B and the source of the MC. There were no other obvious CMEs that occurred between 13 and 18 January 2010. Although the $\approx$ six-day travel time to ST-B seemed very slow, it was a good match with the ≈ 320 km s^{-1} solar-wind speed measured *in situ* during the MC. In addition, this association was confirmed by heliospheric imaging from the STEREO/*Sun Earth Connection Coronal and Heliospheric Investigation* (SECCHI: Howard *et al.*, 2008) *Heliospheric Imagers* (HIs) in ≈ 1 AU solar orbits (Eyles *et al.*, 2009; Harrison *et al.*, 2012) and the *Solar Mass Ejection Imager* (SMEI) in Earth orbit (Eyles *et al.*, 2003; Jackson *et al.*, 2004). The heliospheric imaging combined with the near-Sun imaging and 3D modeling allowed us to track the dense material through the heliosphere to 1 AU and infer the connection between the 14 – 15 January CME and the 21 January ICME/MC at ST-B. Several reconstruction models are used to understand the 3D geometry and propagation of the CME, and several independent flux-rope model fits are compared with the launch observations and magnetic-field orientations.

The event of 17 January was interesting in its own right, but is not discussed in detail here. Its importance lay in the multiwavelength observations with rapid time-cadences of near-limb observations of a CME and its manifestations, particularly a wave, in the low corona, and in the evolution of the active region, which subsequently became a source of significant space weather at Earth. The CME revealed an unusual circular profile as viewed by ST-B and was also observed over the southeast limb from the SOHO/*Extreme Ultraviolet Imaging Telescope* (EIT: Delaboudinière *et al.*, 1995) and the *Large Angle and Spectrometric Coronograph* (LASCO: Brueckner *et al.*, 1995), appearing as a partial halo to the South from both LASCO and COR2-A. Based on our analysis, it is likely that these were back-side partial-halo views of the CME from these two spacecraft. These copious observations have sparked several articles focused on the origin and driving of the coronal wave and its relation to the CME (*e.g.* Veronig *et al.*, 2010; Grechnev *et al.*, 2011; Zhao *et al.*, 2011; Muhr *et al.*, 2011; Temmer, Vrsnak, and Veronig, 2013).

This article is organized as follows: Section 2 provides an overview of the instrumentation available and the resulting observations and measurements made during this period, with emphasis on the heliospheric imaging and *in-situ* aspects. Section 3 describes the heliospheric imaging observations and 3D density reconstructions that we used. In Section 4 we discuss the *in-situ* measurements of the ICME at ST-B, including boundary layers and flux rope fits to the MC. We summarize and conclude in Section 5. We also include 11 movies (M) as supplementary material for the online version of this article. M1 and M2 show EUVI-B images of the erupting filament (304 Å) and the arcade (171 – 195 Å composite). M3 and M4 show enhanced LASCO-C2 images of the CMEs on 15 and 17 January. Movies related to the reconstructions in Section 3.1: high-resolution SMEI 3D density reconstruction images run with a constant solar-wind velocity of 320 km s^{-1} during this period as a fish-eye

view (M5), in the Ecliptic plane (M6), and in a meridional plane that includes the Sun, ST-B, and the Ecliptic poles (M7); M8 is a movie of images using the same reconstruction images to trace back the SMEI-observed material to the field of view (FoV) of LASCO-C3 on 15 and 17 January. Movies related to the reconstructions in Section 3.2: M9 shows SECCHI-A images of the 14 – 15 January CME with tracking markers, M10 shows real and simulated SECCHI images of the CME based on a thin-flux-rope model, M11 shows the same for LASCO-C3 images. The techniques used for making the movies are described in each section. The online supplementary material also includes plots of the plasma and magnetic-field data from the *Wind* spacecraft at L_1 from 19 – 23 January 2010 and from MESSENGER in Mercury's orbit from 14 – 23 January 2010.

2. Overview of Solar and Heliospheric Instruments, Observations, and Measurements

The events of January 2010 were observed remotely by EUV and white-light telescopes onboard the twin STEREO spacecraft in 1 AU orbits, SOHO at L_1, and by the heliospheric imagers of SMEI in Earth orbit and on the STEREOs. LASCO consists of two operating coronagraphs: C2 with a FoV of 1.5 – 6 $R_\odot$ and C3 with a FoV of 3.7 – 30 $R_\odot$. The SECCHI package on each STEREO spacecraft consists of the *Extreme Ultra-Violet Imager* (EUVI), two coronagraphs (COR1 with a FoV of 1.4 – 4.0 $R_\odot$ and COR2 with a FoV of 2.5 – 15 $R_\odot$), and the HI instruments, HI-1 and HI-2. In mid-January 2010, ST-B and ST-A were located 69.9° East and 64.4° West of Earth, respectively, and they were separated 134.3° from each other, as illustrated in Figure 1. The expected radial trajectories of the two CMEs discussed here are shown by the arrows in panels a and b; panel c shows the Ecliptic-plane view on 21 January at 00 UT when the magnetic cloud arrived at ST-B. The EUVI obtains full-disk solar images in four EUV wavelengths, producing images with a cadence as fast as 2.5 minutes in the most commonly observed wavelength band (171 Å).

The SECCHI-HI telescopes view the inner heliosphere starting at an elongation of 4° from the Sun. HI-1 has a FoV of 20°, from 4 – 24° elongation ($\approx$ 12 – 85 $R_\odot$), and HI-2 of 70°, from $\approx$ 19 – 89° elongation ($\approx$ 68 – 216 $R_\odot$). There is a 5.3° overlap between the outer HI-1 and inner HI-2 FoV. The HIs do not cover the entire position angle (PA) range around the Sun, but observe up to a 90° range in PA, nominally centered on the Ecliptic and at this time viewed either East (HI-A) or West (HI-B) of the Sun–Earth line. Launched in January 2003 on the *Coriolis* spacecraft, SMEI imaged nearly the entire sky beyond 20° elongation in white light once per 102-minute spacecraft orbit, using three baffled camera systems. It was deactivated in September 2011 and during its 8.5-year lifetime observed $\approx$ 400 CMEs. See Howard *et al.* (2013) and references therein for further details on the SMEI science accomplishments.

Pertinent spacecraft *in-situ* data available for this period include the ST-B measurements, which are described in detail in Section 4 (see Figure 14), *Wind* and the *Advanced Composition Explorer* (ACE) around the Sun–Earth L_1 point, and the *MErcury Surface, Space ENvironment, GEochemistry, and Ranging* (MESSENGER: Domingue and Russell, 2007) spacecraft, which lagged Mercury in its orbit (see Figure 1). At this time Venus was behind the Sun and Mars was behind the Earth, therefore instrument data from the spacecraft orbiting those planets are not useful for this period.

MESSENGER, in its close orbit to the Sun, moved much faster than the other spacecraft. During this period, MESSENGER moved from $\approx -55°$ to $-22°$ heliographic longitude (relative to the Sun–Earth line), or over a $\approx$ 33° span, between 15 and 21 January. Its angular distance from ST-B increased from only 15° on 15 January to 48° on 21 January. The ACE

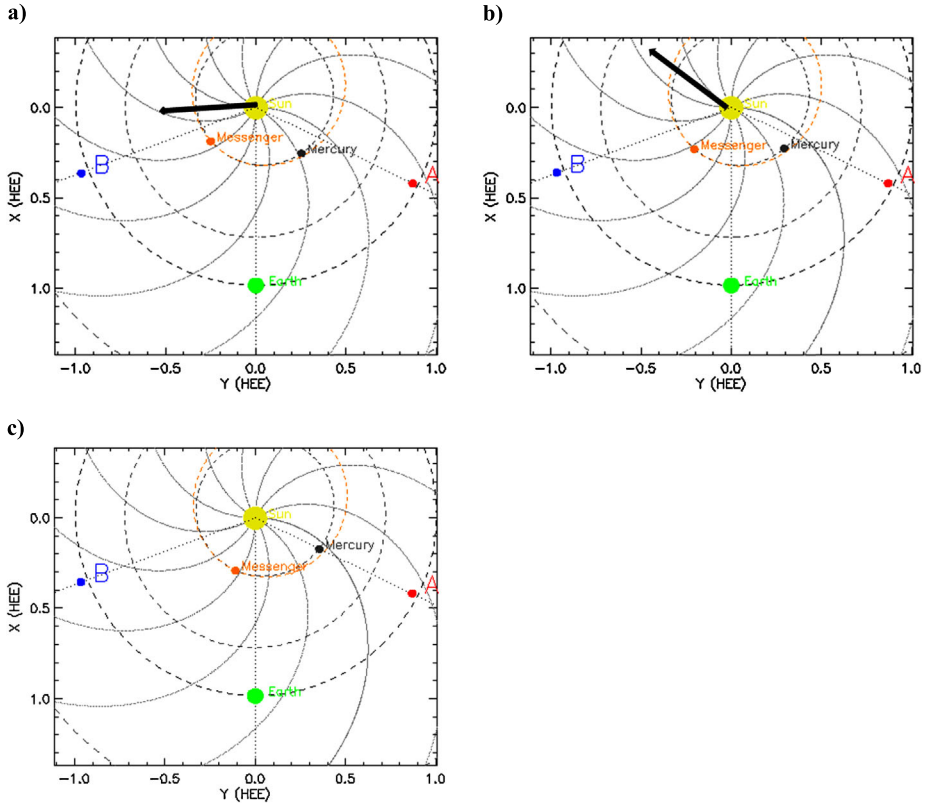

Figure 1 Ecliptic-plane views of the location in Heliocentric Earth Ecliptic (HEE) coordinates of STEREO-A (A), -B (B), Earth (L_1), MESSENGER, and of the inner planets Earth and Mercury and their orbits (dashed lines). (a) Arrow indicates the longitudinal direction of the first CME on 15 January 2010 00 UT; (b) arrow denotes the longitudinal direction of the second CME on 17 January 04 UT; and (c) the view on 21 January 00 UT when the magnetic cloud arrived at ST-B. At this time, ST-A and ST-B were 134° apart. Note that MESSENGER was not in orbit at Mercury, but traveled a significant distance during this period. These plots are generated at the STEREO Science Center site: stereo-ssc.nascom.nasa.gov/cgi-bin/make_where_gif. The Parker-spiral field lines for average solar-wind speed are shown.

and *Wind* data at L_1 showed evidence of a moderate fast-slow stream interaction region during this period, but no obvious large-scale transients. There were density and magnetic-field enhancements on 20 January, but these could have been due to stream-interaction compressions. Although during this period MESSENGER only obtained magnetic-field data (Anderson *et al.*, 2007), there may have been a small MC-like structure on 17 January, onset $\approx$ 04 UT with duration $\approx$ ten hours. If the 14 – 15 January CME had a speed of 320 km s^{-1} (see later), it would take about 1 2/3 days to reach MESSENGER. The MESSENGER structure was delayed by about half a day from this arrival time. Only the western flank of the CME might have grazed MESSENGER but, without plasma data, we can say no more about this *in-situ* feature. There was no shock or any other obvious transient observed by MESSENGER from 14 – 23 January. We conclude that at neither L_1 nor MESSENGER were there obvious transients that we could clearly associate with the ST-B MC on 21 – 22 January. We include both the MESSENGER and *Wind in-situ* plots in the supplementary material for completeness.

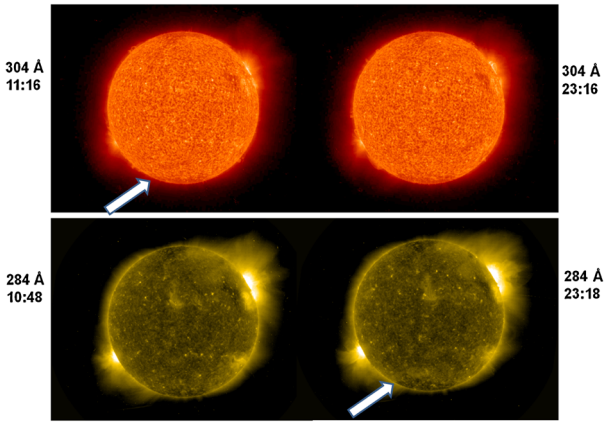

Figure 2 The 14 – 15 January 2010 event viewed from EUVI-B. The top images are in 304 Å and show the southern pre-existing filament that erupted (top left arrow) and swept outward and westward. Soon after, an arcade appeared in the original filament channel, as clearly seen in the bottom 284 Å image (bottom right arrow).

The first of the two CMEs considered here was narrow ($\approx 60°$), but well formed with a dark, circular interior suggestive of a flux rope. When first detectable in LASCO-C2, on 14 January at 21:17 UT, it was nearly centered on the solar east-limb Equator (Figure 1a shows the radial trajectory). The void first appeared at 22:58 and was clearly visible by 23:58 UT. In LASCO-C3, viewing farther out, the void was clearly visible on 15 January, 08:15 UT. The online CDAW (cdaw.gsfc.nasa.gov/CME_list/index.html) CME onset is listed as 14 January, 22:42 with a slow linear speed of 203 km s^{-1}, a peak second-order speed of 377 km s^{-1}, and an acceleration of 57 m s^{-2}. The CME was also viewed by the SECCHI-A CORs, first by COR1-A with onset on 14 January, 20:45 UT, then by COR2, onset around 03:00 on January 15. The CACTus COR2 catalog (sidc.oma.be/cactus/) lists an onset of 15 January 03:24 with an average speed of 178 km s^{-1}.

Unlike the 17 January eruptive flare, the activity associated with the very slow 14 – 15 January CME was fairly faint and subtle. It was associated with a large erupting filament centered on the southern hemisphere as viewed by EUVI-B. Figure 2 shows the filament in 304 Å (top-arrow) that began to rise at about 11:00 UT, then rapidly moved out and westward across the disk starting about 18:00 UT (see also Movie M1). Later at $\approx$ 19:00 UT, an arcade appeared in the original filament channel, as clearly seen in the 284 Å image (bottom-arrow, see also Movie M2). From SOHO the filament was observed in EIT 304 Å at PA = 133° rising between the images taken six hours apart on 14 January, 07:20 and 13:20 UT, and then not there by the 15 January, 01:21 image. In EUVI-A 304 Å the filament eruption appeared as a double structure, rising and looping equatorward from 14 January 17:00 to 15 January $\approx$ 05:00. In the EIT 195 Å coronal images, the arcade in this same region was first visible at 14 January 20:09 UT. During this time in EIT, both the filament and coronal structures could be observed moving equatorward as the filament rose, a motion also observed in the earliest COR1-A images (see Movie M9). The arcade structure and motion are not very clear in EUVI-A coronal images, possibly because it was too far East to be clearly observed from ST-A. By the time the CME was observed in both LASCO-C2 and COR2-A, it was at PA $\approx 90°$ and moved radially outward from that position. The early equatorward motion of eruptions is often observed (*e.g.* Cremades and Bothmer, 2004) and has been simulated (*e.g.* Zuccarello *et al.*, 2012).

The more energetic 17 January flare–CME was first observed at 03:51 UT from a ST-B disk location of S25° E59°. The CME was wider ($\approx 125°$) and launched farther South (PA $\approx 115°$) than the 14 – 15 January CME. Figure 3 shows enhanced LASCO-C2 coronagraph images of the two CMEs during this period, the first beginning late on 14 January and the

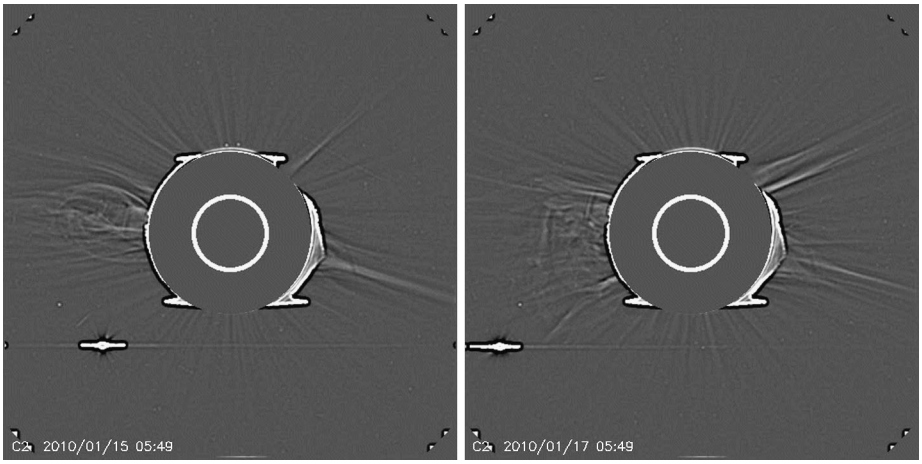

Figure 3 Comparisons of single wavelet-enhanced frames from movies of the 14 – 15 (left) and 17 January (right) 2010 CMEs viewed from the LASCO-C2 coronagraph. The axis of the 14 – 15 January CME was slightly north and of the 17 January CME slightly south of the equator. The bright object below and east of the occulting disk is Venus. The LASCO and EIT images have been enhanced using a technique developed by Stenborg (Stenborg and Cobelli, 2003).

other early on 17 January. The first of these was a slightly brighter and compact CME moving outward to the solar East and the second CME, a partial halo in C2, was brightest to the solar East and Southeast in the C2 images. Note the appearance of circular voids, suggestive of flux ropes, in both events (see also Movies M3 and M4). Finally, late (20:49 UT) on 18 January, a third CME erupted over the ESE limb viewed by LASCO. This CME is mentioned here for two reasons: i) As an X-ray C5 flare, it was the harbinger of rapid, intense flare and CME activity from Region 11041 as it approached the Earth-facing disk; and ii) it likely evolved into the trailing material viewed in SMEI 3D reconstructions and arriving *in-situ* at ST-B on 23 January (see next section).

3. Heliospheric Imaging and Modeling: 3D Density Reconstructions

3.1. SMEI CME 3D Density Reconstruction

The analysis of the white-light heliospheric images from SMEI employed here follows the University of California, San Diego (UCSD) 3D computer-assisted tomography (CAT) analysis chain as developed by, *e.g.*, Jackson *et al.* (2006, 2010a, 2010b, 2011, 2013), Bisi *et al.* (2008), and Jackson (2012). The UCSD technique determines the 3D extent of heliospheric structures by using the line-of-sight response in Thomson-scattered light, and iteratively fitting these from limited viewing locations. Currently, the reconstruction incorporates a purely kinematic solar-wind model. Given the velocity and density on an inner boundary, a 3D solar-wind model is derived by assuming radial outflow and enforcing conservation of mass and mass flux. If the wind model does not match the overall observations, the source-surface values are altered to minimize the deviations and achieve a best fit. The SMEI 3D reconstructions have standard 6.7° latitude and longitude spatial resolutions, with a 0.5-day temporal resolution. An initial velocity typical of the average solar-wind speed is usually used for SMEI density reconstructions, but in this case a slower constant velocity of 320 km s^{-1}

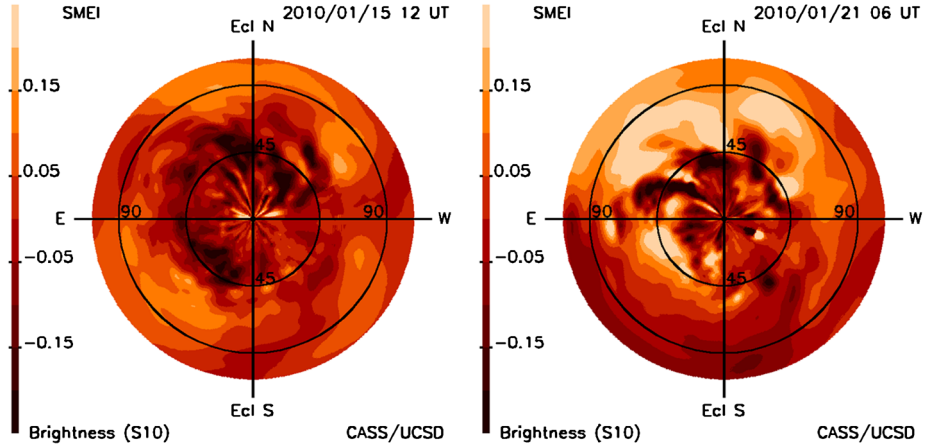

Figure 4 SMEI fish-eye difference images that reveal fainter structures. The circles denote angular distances (elongation) of 45° and 90° from the Sun. At this time, ST-B was at ≈ 55° elongation East of Earth along the Ecliptic (E–W) line. Left: 15 January, 12 UT after the launch of the 14 January CME. Right: 21 January, 06 UT during the magnetic cloud interval at ST-B. In the intensity scale [S_{10} units] negative differences are darker. The difference images have the previous reconstructed 3D volume subtracted from the current 3D volume. The 3D-volume reconstructions have a cadence of 12 hours.

was used to match the average velocity observed within the MC at ST-B. As noted in Section 1, the online SMEI reconstruction movies, M5 – M8, show these images over the period of 14 – 26 January.

Figure 4 shows two fish-eye difference-image views from the SMEI 3D reconstructions (see also Movie M5). A fish-eye projection is a zenithal equidistant projection in which the distance along a radius from the Sun is a straight line. The maps are in heliocentric Ecliptic coordinates, *i.e.* the Equator of the map is the Ecliptic plane, and the circles are in angular distance from to the Sun. These are chosen to represent the time on 15 January (about a half-day after the 14 January CME erupted) and when that CME was at the ST-B spacecraft on 21 January. In the 21 January image, some of the late-18 January CME (as noted) is likely observed to the South and East of the Sun–Earth line. Note the looplike structure that extended to the Ecliptic plane along the line of sight to ST-B on 21 January. Some of this material was likely associated with the 14 January CME, but most of the material was to the North. There was a pre-existing streamer in the coronagraph observations that was pushed northward by the CME (see Figure 3 and movie M3), and this material may be the northern structure highlighted in the SMEI difference images.

Figure 5 shows an Ecliptic cut (left) and a meridional cut (right) from the SMEI 3D reconstructions displaying the reconstructed structure that is part of the 14 January CME when it was at the ST-B spacecraft on 21 January (see also Movies M6 and M7). The CME is the dense (darker) region at 1 AU and reaching ST-B on 21 January. Note that most of the material was to the *East* of ST-B. The meridional view shows that the densest part was north of the Ecliptic plane. The material not yet at 1 AU and between Earth and ST-B was possibly associated with the late-18 January CME. Figure 6 is a remote-observer view of the 14 January CME when it was engulfing the ST-B spacecraft on 21 January. The ST-B location is indicated, but it is obscured by the CME. As shown in Figure 5, there was material North of the Ecliptic plane and in the Ecliptic most of material was *East* of the Sun–ST-B line.

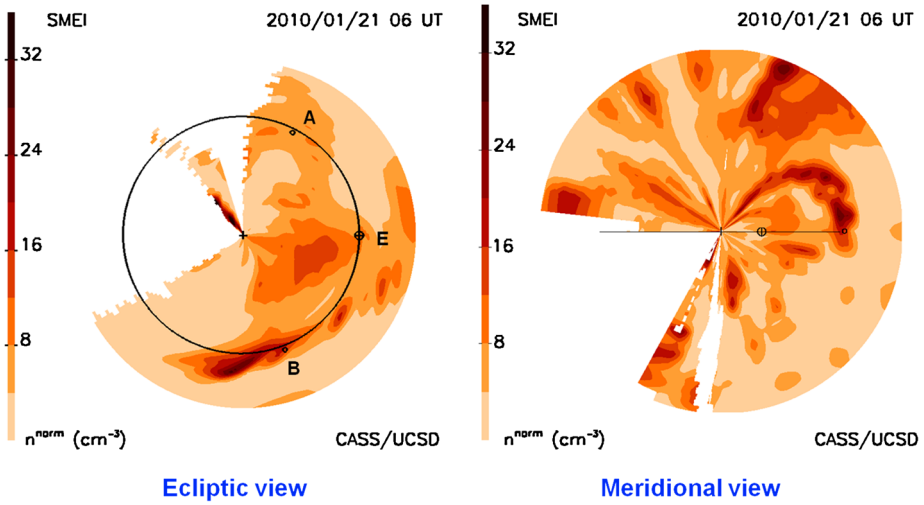

Figure 5 Ecliptic cut (left) and meridional cut (right) of the SMEI 3D-reconstructed densities showing the structure on 21 January. The positions of ST-A (A), Earth, and ST-B (B) are marked on the Ecliptic view and of ST-B and Earth on the meridional view, a cut through the ST-B–Sun–Ecliptic pole plane. The intensity scale is scaled as NpR^{-2}, with increasing density being darker. The white areas denote regions of poor or absent data coverage.

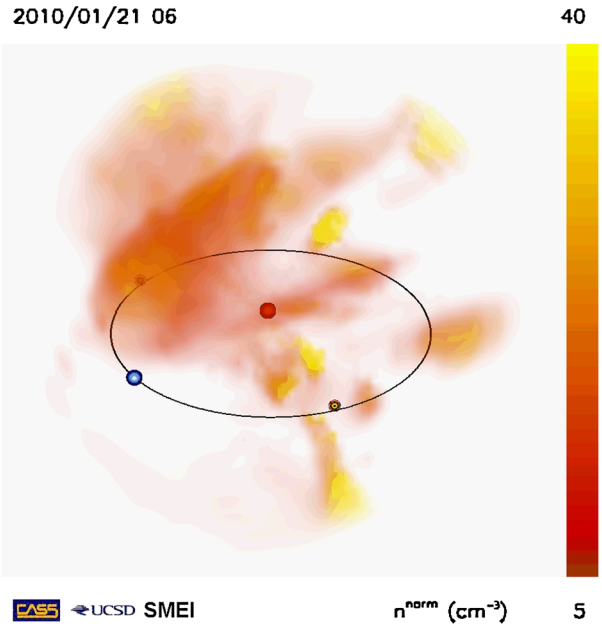

Figure 6 A remote view of the SMEI 3D reconstructed density [NpR^{-2}] structure from above the Ecliptic plane on 21 January, 06 UT, during the magnetic-cloud interval at ST-B (see Figure 14). The Sun is red, the Earth blue, and the black circle is the 1 AU orbit. The locations of the STEREO spacecraft are circled; ST-A West (right) of Earth and ST-B to the East and obscured by the CME.

We also were able to use the SMEI reconstructions to trace back the heliospheric-density patterns at a speed of 320 km s^{-1}, the velocity of the MC at ST-B, to provide a view similar to that observed in the LASCO coronagraphs. This trace-back technique (Jackson, 2012) works well in this case, because the signal-to-noise ratio of the SMEI data was good and

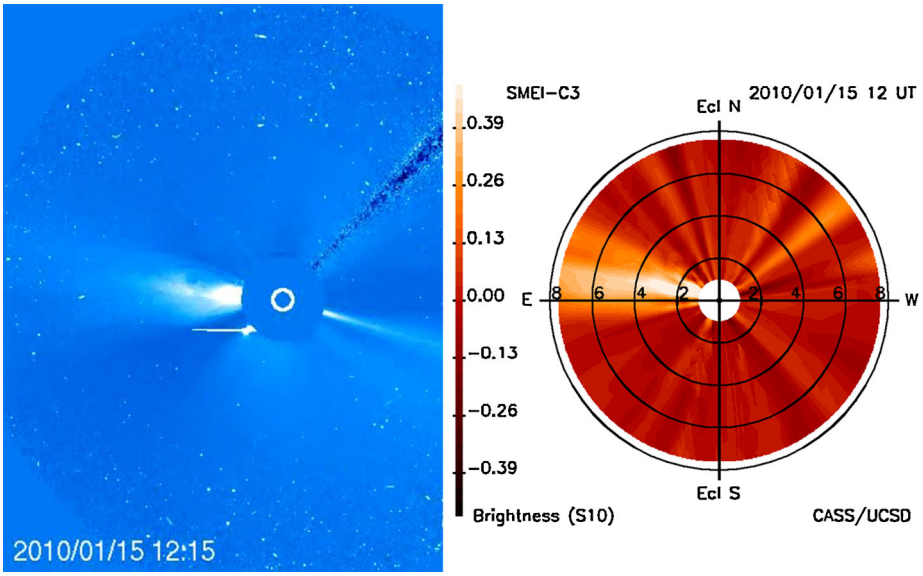

Figure 7 Comparison of LASCO-C3 image of the 14 – 15 January CME (left) with a "trace-back" of 3D-reconstructed material from SMEI to 2.5 $R_{\odot}$ at the same time (right). These pseudo-coronagraph brightness images [in S_{10} units] are differences wherein a data-cube volume 12 hours prior to the current image is subtracted from the previous image. The SMEI trace-back image shows the solar disk in white, equivalent to the white circle in the C3 image. The black circles are distance in solar radii from the Sun center. Adapted from Jackson (2012).

there was only very little acceleration/deceleration of the CME near the Sun. Figure 7 shows the similarity of the traced-back reconstruction to the 14 – 15 January CME observed by the C3 coronagraph that erupted from the Sun in the reconstructions at about the correct time (see also Movie M8). The coronagraph brightness is decreased in its inner portion near the Sun because of vignetting of the inner field of the image. The SMEI pseudo-coronagraph observations approximately match this vignetted brightness fall-off through use of an r^{-2} density fall-off imposed on the volumetric analysis. This direct LASCO–SMEI comparison provides qualitative confirmation that the material that we tracked in SMEI toward ST-B was the same CME observed near the Sun by LASCO.

At ST-B, the SMEI 3D reconstructions are well correlated with the ST-B *Plasma and Suprathermal Ion Composition* (PLASTIC: Galvin *et al.*, 2008) *in-situ* density measurements, as shown in Figure 8. This *in-situ* fit during the event provides good assurance that the density structure reconstructed in 3D has the actual shape of the CME at the ST-B location. The cross-correlation over an extended interval of 16 days, from 15 – 30 January, is very good: −0.78. During the period of interest, there were two periods of density enhancements, in mid-21 January and from 23 January. The first was likely associated with the 14 – 15 January CME, the second with the late-18 January CME (see Figure 5a and movie M6). The density enhancement at ST-B was located in the middle of the MC on 21 January, thus allowing the general 3D orientation of the ICME structure to be determined (see Section 4 and Figure 14). The derived SMEI peak density is 16 cm^{-3} (Figures 5 and 8), consistent with, but slightly higher than, the peak *in-situ* proton density measured at ST-B (Figure 14). This slight discrepancy is not surprising given the coarser averaging required for the 3D reconstruction *vs*. the high-resolution *in-situ* measurements.

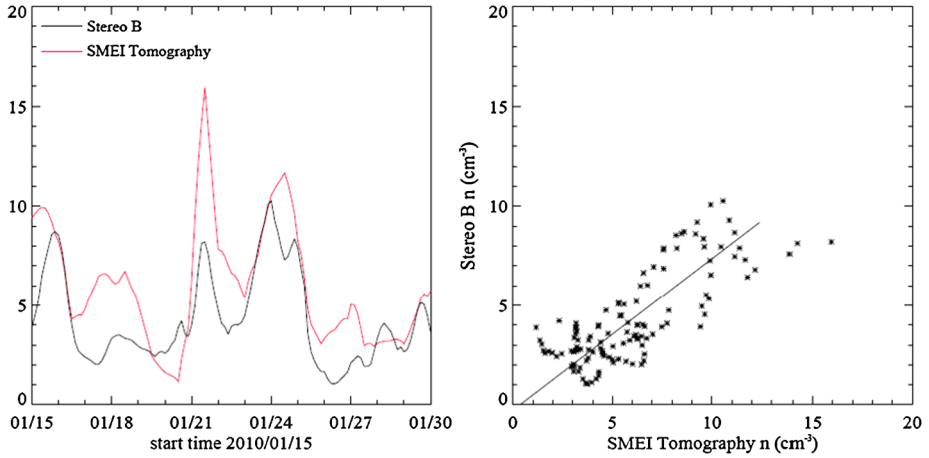

Figure 8 (Left) Correspondence of SMEI 3D-reconstructed (using constant 320 km s^{-1} solar-wind speed) densities (red line) and the STEREO *in-situ* densities from PLASTIC (solid black line). (Right) Cross-correlation of the two sets of densities over 16 days. The spacecraft densities have been averaged with a 0.5-day boxcar average to match the SMEI analysis.

3.2. 3-D Flux-Rope Reconstruction of the CME

Figure 9a shows various views of the 14 – 15 January 2010 CME from the ST-A, ST-B, and SOHO/LASCO perspectives (see also Movies M9, M10, and M11). The images are displayed in running-difference format, where the previous image is subtracted from each image to subtract the static background and emphasize the dynamic CME front. The CME presents a circular appearance in ST-A images, particularly in the HI1-A image in Figure 9a. Circular structures such as these have often been interpreted as flux ropes observed edge-on (Chen *et al.*, 1997; Wood *et al.*, 1999; Cremades and Bothmer, 2004; Krall, 2007). Thernisien, Vourlidas, and Howard (2009) demonstrated that a flux-rope morphology is consistent with COR2 observations of a number of CMEs, and Vourlidas *et al.* (2013) presented observations and simulations showing that at least 40 % of LASCO CMEs have a clear flux-rope structure. Wood and Howard (2009) developed a technique to empirically reconstruct the 3D density distributions of CMEs that can be modeled as flux ropes, which has been applied to many events observed by STEREO and LASCO (*e.g.* Wood, Howard, and Socker, 2010; Wood *et al.*, 2011). This approach uses trial-and-error modeling, where a parameterized 3D flux-rope structure is constructed and used to generate synthetic images, and then the parameters of the model are adjusted to maximize agreement between the real and synthetic images. Mass is placed only on the surface of the 3D flux rope, with nothing assumed in the interior, which means that this approach only models the basic outline of a flux-rope CME.

The 14 – 15 January 2010 CME was reconstructed using these techniques. First, a kinematic model is necessary to establish the size scale of the morphological reconstruction as a function of time, which is then used to generate the synthetic images that are compared with the real STEREO and LASCO data. We assumed that the CME expands in a self-similar fashion, meaning its shape does not change with time, only its size. The kinematics of a CME are best measured from a lateral perspective, from which the CME's radial expansion results in motion within the image plane. Unfortunately, with the 14 – 15 January 2010 CME being directed roughly toward ST-B, neither ST-A nor -B has such a perspective.

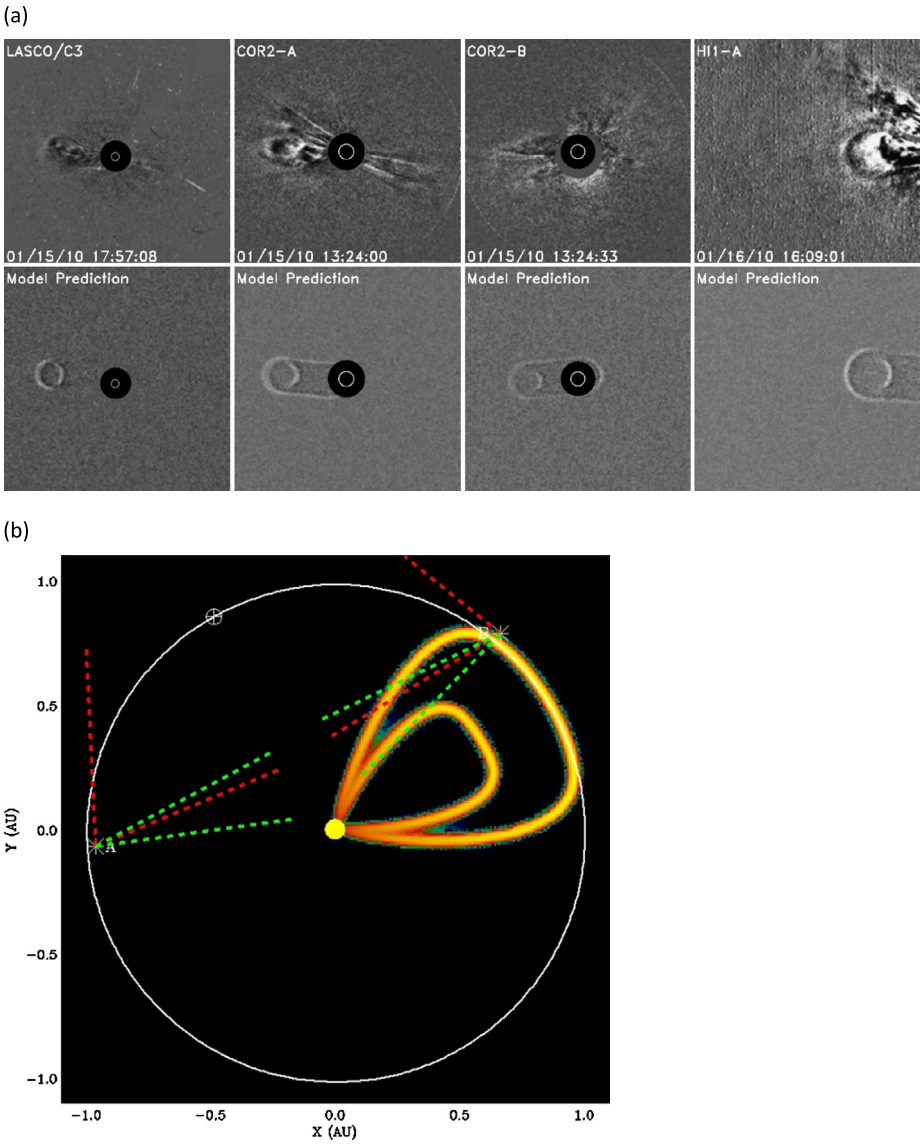

Figure 9 (a) 3D density reconstruction of the 14 January CME–flux rope using the Wood technique (Section 3.2). The top panels show four images of the 14 – 15 January 2010 CME as observed from four white-light telescopes on the SOHO (LASCO-C3), ST-A (COR2-A, HI1-A), and ST-B (COR2-B) spacecraft. The clear circular appearance of the CME, especially from SECCHI-A, is interpreted as a flux rope observed nearly edge-on and modeled as such. The CME is very faint from the frontal perspective of ST-B and is only clearly detected, as a faint halo, in COR2-B. The bottom panels show synthetic images computed based on the 3D CME reconstruction described in Section 3.2 for comparison with the actual images above. (b) The Ecliptic–plane geometry of the 14 – 15 January 2010 CME-flux rope. The locations of Earth, ST-A, and ST-B in the Ecliptic plane are shown in Heliocentric Aries Ecliptic (HAE) coordinates. The green and red dotted lines indicate the fields of view of the HI1 and HI2 imagers, respectively, on ST-A (left) and ST-B (right). Also shown is an Ecliptic-plane slice through the 3D-reconstructed flux rope of the 14 – 15 January CME as it approached ST-B on 20 January (see Section 3.2).

ST-B viewed the CME from the front and one side, and ST-A viewed it from behind (see Figure 9b). LASCO had the best perspective, but its imagers can only view near the Sun. SMEI, in Earth orbit, had a better lateral perspective, and those results are described in the previous section. For this kinematic analysis, we are limited to the ST-A observations, despite the less-than-ideal viewing geometry. Note that for ST-A the CME was indistinct when it reached the HI2-A FoV, therefore we only tracked its front through the HI1-A FoV.

In ST-A images, we follow the leading edge of the CME, measuring its elongation angle from Sun-center [ε] as a function of time. These angles must be converted into actual distances [r]. Two methods were originally used, the point-P and fixed-φ methods (Webb *et al.*, 2006; Kahler and Webb, 2007; Howard *et al.*, 2007; Howard, Nandy, and Koepke, 2008; Sheeley *et al.*, 2008; Wood *et al.*, 2009). The former assumes a very broad spherical front centered on the Sun, and the latter a narrow CME. More recently, Lugaz, Vourlidas, and Roussev (2009) proposed a third method, which approximates the CME as a sphere centered halfway between the Sun and the CME's leading edge. This assumption yields $r = 2d$ $\sin \varepsilon/[1 + \sin(\varepsilon + \varphi)]$, where d is the distance from the observer (ST-A in this case) to the Sun, and φ is the angle between the CME trajectory and the observer's line of sight to the Sun. Lugaz, Vourlidas, and Roussev (2009) called this the harmonic-mean approximation, since an r-value computed under this assumption represents the intermediate harmonic mean of values computed under the other two approximations. From the morphological part of the analysis described below we determine $\varphi = 152°$.

The top panel of Figure 10a shows our distance-*vs*.-time results for the 14 – 15 January 2010 CME computed using the harmonic-mean approximation. These points are fitted with a simple three-phase kinematic model that we used in the past to model the 1 June 2008 CME (Wood, Howard, and Socker, 2010), a similar CME with a very slow initial speed. The model assumes an initial phase of constant velocity [V_1] ending at some time t_1; a second phase of constant acceleration [a_2] ending at some time t_2; followed by a final phase of constant velocity. In addition to these four free parameters, there is a fifth involving a time shift from the model time vector to that of the actual measurements. Figure 10a shows the best fit to the data based on this simple five-parameter model, with the lower two panels showing the velocity and acceleration of the CME according to the fit. The modeled CME accelerates from 54 km s^{-1} at a Sun-center distance of 3.0 $R_\odot$ to 316 km s^{-1} at 15.8 $R_\odot$, and then it maintains that speed to 1 AU. Its time of arrival at ST-B is $\approx$ 19:40 UT on 20 January, which is roughly consistent with the *in-situ* data.

With this kinematic model we can expand a morphological model with time, and the morphological reconstruction can proceed. We refer to Wood and Howard (2009) for details about the methodology behind the creation of 3D flux-rope shapes. Figure 10b shows the 3D flux-rope shape that we derive for the 14 – 15 January 2010 CME, and Figure 9b shows a slice through this model in the Ecliptic plane. The flux rope has an E–W orientation within the Ecliptic plane, but the west leg is tilted above the Ecliptic plane by 5°. The CME trajectory is 152° East of ST-A, hence the φ value assumed above, or 18° *East* of ST-B. This is consistent with the UCSD SMEI analysis above, which shows that most of the CME material in the Ecliptic lay in an East–West band that was mostly to the *East* of the location of ST-B (Figure 5). ST-B is struck by the west side of the flux rope, as shown explicitly by the arrow in Figure 10b.

The bottom panels of Figure 9a show synthetic images computed from the 3D reconstruction for comparison with the real images. As mentioned above, the arrival time of the CME at ST-B is well matched by this reconstruction, but the encounter duration at ST-B would be about two days, significantly longer than the $\approx$ one-day ICME encounter measured in the *in-situ* data (Figure 14). This implies a significantly thinner flux rope than the one modeled in Figures 9b and 10b.

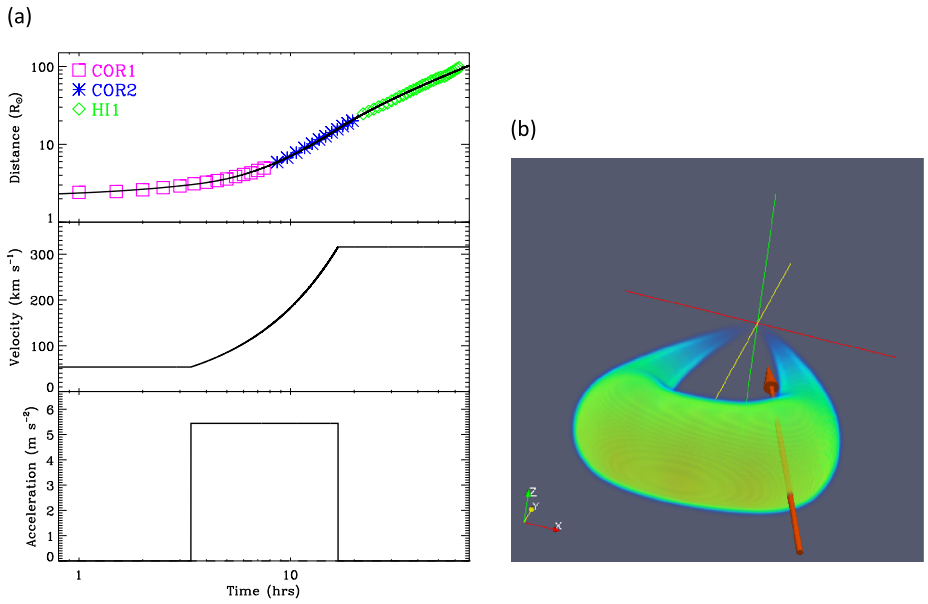

Figure 10 (a) Based on the technique discussed in Section 3.2, this shows the best-fit kinematic model of the leading edge of the 14 January 2010 CME. The top panel shows distance measurements of the leading edge of the 14 – 15 January CME based on images from ST-A as a function of time, where $t = 0$ is 14 January 20:45 UT. These measurements are fitted with the three-phase kinematic model described in Section 3.2. The fit is shown as a solid line in the top panel, and the bottom panels show the velocity and acceleration of the CME suggested by this fit. (b) A 3D reconstruction of the 14 – 15 January CME based on images from ST-A, ST-B, and LASCO, assuming a flux-rope geometry. The red arrow indicates ST-B's passage through the structure assuming a simple self-similar expansion for the CME.

Perhaps the most novel aspect about this CME reconstruction concerns the part of the CME that produced the circular rim in ST-A images. Such circular structures are often seen in images of CMEs and, as mentioned earlier, are being interpreted as flux ropes viewed edge-on. However, ST-A's viewing angle here is such that it is not the apex of the flux rope that is producing the circle, but the west leg of the flux rope viewed from behind the Sun (relative to the CME's trajectory). Thus, the CME's apparent progression outward from the Sun from ST-A's perspective is not so much the outward radial propagation of the flux-rope apex, but instead the lateral westward expansion of the west leg of the flux rope. This distinction is most apparent in Figure 9b, which shows that the west flux-rope leg is observed by ST-A, moving away from the east limb of the Sun.

Figure 11 is an Ecliptic plane map of elongation vs. time of STEREO HI-A brightness for nine days surrounding the 14 – 21 January events. Such time-elongation profiles, also called j-maps, have been used to evaluate the kinematics of CMEs (*e.g.* Sheeley *et al.*, 1999; Rouillard *et al.*, 2008; Davies *et al.*, 2009; Tappin and Howard, 2009; Harrison *et al.*, 2012). They show the locus of points along the lines-of-sight from outward-moving structures, but not the solar distance of the structure at any given radius. The tracks in Figure 11 are from difference images and track features passing from the Sun through the HI1-A FoV in the lower panel, then HI2-A in the large upper panel. In these maps CMEs appear as straighter lines, whereas corotating interaction regions (CIRs) are more curved. The yellow bar indicates the duration of the ICME proton-density enhancement at ST-B on 21 January (Figures 8 and 14), and the elongation of the ST-B spacecraft as viewed from ST-A is 23.75°

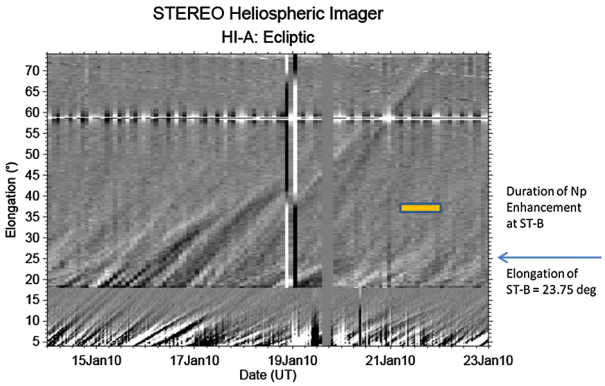

Figure 11 Ecliptic-plane map of elongation *vs*. time of HI-A brightness from 14 – 23 January 2010. These are from difference images and track features passing from the Sun through HI1-A in the lower panel, then HI2-A in the large upper panel. The yellow bar indicates the duration of the proton-density enhancement at ST-B on 21 January, and the angular elongation of the ST-B spacecraft as viewed from ST-A is 23.75° as denoted by the blue arrow. The Earth is the horizontal bright track at $\varepsilon = 58°$; vertical dark or bright lines or bars are data gaps. Courtesy of J. Davies, RAL.

as denoted by the blue arrow (see Figure 11). The faint, broad enhancement crossing this elongation on 21 January is most likely the track of the dense portion of the ST-B ICME (see also Movie M9). Unfortunately, the trace of this structure observed in HI2-A cannot be unambiguously identified earlier in the HI1-A data.

3.3. Multimethod CME 3D Reconstruction from Coronagraph Data

Images from the SECCHI-COR2 and LASCO-C3 coronagraphs for the 14 – 15 January CME were analyzed to estimate its near-Sun geometry, axis direction of propagation, speed, dimensions (height and width), and mass using a combination of four independent techniques. The techniques used were geometric localization (Pizzo and Biesecker, 2004; de Koning, Pizzo, and Biesecker, 2009), polarimetric localization (de Koning and Pizzo, 2011), the assumption that CME mass is independent of the viewing perspective (Colaninno and Vourlidas, 2009), and a three-view reconstruction technique based on visually matching the projection of a 3D shape to the CME outlines observed by STEREO and SOHO. The three-view reconstruction tool, called CME analysis for research purposes (CARP), is an expanded, research-grade tool based on the CME analysis tool (CAT), which was created specifically for CME forecasting at the NOAA *Space Weather Prediction Center* (Millward *et al.*, 2013).

Geometric reconstruction uses a series of lines-of-sight from the two STEREO spacecraft to assemble a stack of polygons that are used to characterize the 3D location, velocity, and dimensions of a CME. Polarimetric localization uses the measured polarization fraction within a CME to derive its location relative to the plane of the sky. By applying this technique to both STEREO spacecraft, we determined a unique location for the CME. The direction of propagation for the CME for all four methods is shown in Table 1; all directions are in Heliospheric Ecliptic (HEE) coordinates. Note that the results from polarimetric localization are outliers relative to the other three methods. Therefore, instead of calculating the mean of all of the methods, we calculated the median, which is a well-known, robust estimator of the central location.

Table 1 Direction of propagation of the CME, in HEE coordinates, from the four techniques in Section 3.3. The bottom row is the median of all values and provides a robust estimate for the CME's direction of propagation. The error in the median is the median absolute deviation about the median.

Method	Latitude [°]	Longitude [°]
Polarimetric Localization (ST-A)	-10 ± 4	-62 ± 6
Polarimetric Localization (ST-B)	9 ± 7	-137 ± 14
Geometric Localization	0 ± 15	-86 ± 9
Mass Analysis	n/a	-92 ± 5
Three View	3 ± 1	-86 ± 3
Median of all methods	1 ± 3	-86 ± 9

Because the estimated direction of propagation is nearly in the LASCO sky plane, the best estimate of the CME speed is expected to come from LASCO. Linear fitting of the CME leading-edge position observed by LASCO-C3 as a function of time yields a CME speed of 310 ± 20 km s^{-1}. Because of the large angular separation between the STEREO spacecraft, geometric localization provides only a crude estimate of the CME speed: 490 ± 120 km s^{-1}. Despite this, note that the lower end of this speed estimate is consistent with the speed derived from LASCO. The polygon-reconstruction technique employed in geometric localization is also used to obtain a crude estimate of the CME's angular size. For this event, this reconstruction suggests that the CME's East–West half-width is $\approx 23°$, and that the North–South half-width is $\approx 9°$.

By using the robust estimates of CME direction and size derived above, we can constrain the range of possible shapes that is accessible to CARP (including a continuous range of drop shapes from a flat-fronted cone to a lemniscate, with a circular or elliptical cross-section) to obtain a better estimate of the CME characteristics: longitude, $-84° \pm 4°$; latitude, $2° \pm 2°$; speed, 310 ± 20 km s^{-1}; EW half-width, $27° \pm 2°$; NS half-width, $13° \pm 2°$; tilt, $-5° \pm 2°$. The tilt denotes a counter-clockwise rotation around the central axis of the CME; thus, the major axis of the CME is slightly tilted, with the eastern leg of the CME approximately 5° above the Ecliptic and the western leg in the Ecliptic.

Figure 12 shows two representative schematic views of the CME as modeled with these techniques: 12a is a view from slightly above the Ecliptic and east of the Sun–Earth line, and 12b is from the North Pole of the Ecliptic plane. These views can be compared with those from the 3D reconstructions from COR1-A, COR2-A, and HI1-A in Figure 10b and from SMEI out to 1 AU in Figures 5 and 6. To match the three-view and geometric localization widths, it was necessary for the front of the CME to be very flat. This flattened front is also evident in the COR-HI and SMEI results. Physically, this flattening of the CME front could be due to momentum exchange via pressure differences between the CME and MC and the ambient solar-wind flow. Recently, Howard and DeForest (2012a) demonstrated such a flattening observed over the 1-AU travel of a CME observed by the SECCHI telescopes.

The CME mass was also calculated using the standard technique (Vourlidas *et al.*, 2010), which involves converting a properly calibrated, background-subtracted total-brightness image (excess mean solar brightness) to a mass image (grams pixel^{-2}). The total mass estimated along each line of sight depends on the assumed coronal density and the location of the electron-scattering locations relative to the Thomson sphere. For the coronal density we assumed a mixture of 90 % hydrogen nuclei and 10 % helium nuclei, which is a typically assumed coronal mixture. Typically, the electron scattering location is assumed to be in the spacecraft sky plane, yielding a lower limit on the total CME mass. Alternatively, the CME could be regarded as a purely planar structure propagating along a fixed heliographic longitude. By systematically varying the longitude of the CME plane, we can see how the calculated total mass varies with angular distance from the Thomson sphere. An example of this variation is shown in Figure 13. A couple of noteworthy points can be derived from

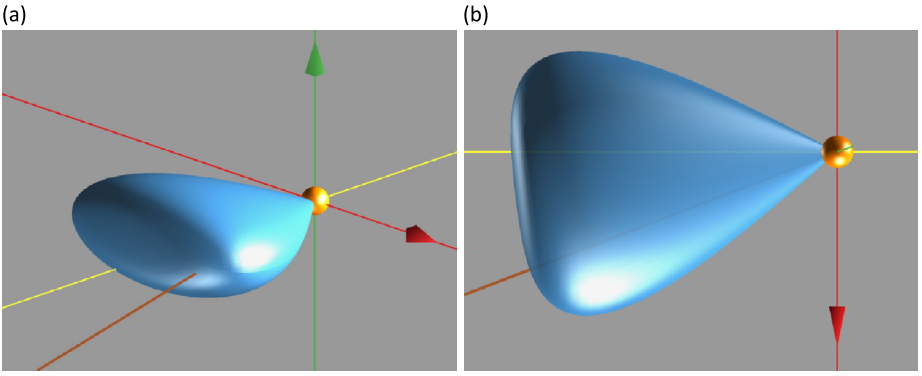

Figure 12 3D reconstruction views of the 14 – 15 January CME near the Sun based on data from the SECCHI and LASCO coronagraphs and using the combination of techniques discussed in Section 3.3. (a) is a view from 4°E and 20°N and (b) is the view from North of the Ecliptic plane. The Sun is the yellow sphere in this HEE coordinate system; the Sun–Earth line is red (arrow toward Earth) and at 0° longitude, the green line and arrow indicates Ecliptic North, and the yellow line is Ecliptic directions 90° East and West of Sun–Earth. The brown line indicates the Sun–ST-B direction. The modeled longitude and latitude of the CME axis are −84° and +2°, respectively, and the CME plane is tilted by −5°.

Figure 13 CME mass analysis. Plot of the CME mass *vs.* HEE longitude for COR2-A (red) and COR2-B (blue) data.

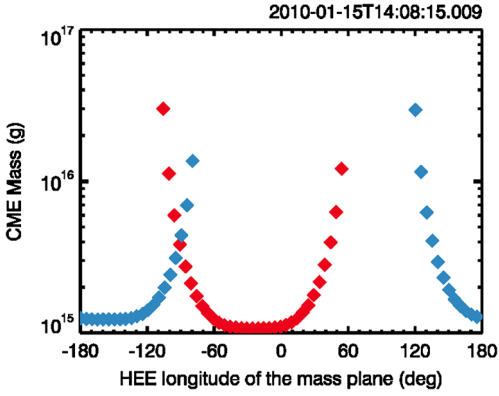

this figure. First, as explained by Colaninno and Vourlidas (2009), since the total CME mass is independent of the observer viewpoint, the plane in which the total CME mass derived from COR2-A imagery equals the total mass derived from COR2-B imagery can be used to estimate the CME direction of propagation; the mass of this planar structure yields an improved estimate of the CME's total mass. According to the information in Figure 13, the total mass for this event is $(3.8 \pm 0.6) \times 10^{15}$ grams and, as mentioned above, its longitude of propagation is $-92° \pm 5°$. This mass is similar to that determined in the CDAW catalog of 2.6×10^{15} grams. The error in the mass and direction are an estimate of the spread in results obtained from repeated analyses of the same data. Second, the figure also clearly shows the effect of the Thomson sphere on the calculation of CME mass. The CME mass is approximately minimum when located within a plane tangent to the Thomson sphere, *i.e.* when it is located within the spacecraft sky plane. The wide trough in the CME mass farther away from the Thomson sphere is evidence of the Thomson plateau described by Howard and DeForest (2012b).

4. *In-situ* Analyses at STEREO-B

4.1. Overview of Measurements at STEREO-B

Figure 14 shows the plasma and magnetic field data acquired by the PLASTIC and the *In-situ Measurements of Particles And CME Transients* (IMPACT: Luhmann *et al.*, 2008) instrument suites on ST-B for the three-day interval 20 – 22 January 2010. From top to bottom the panels show the pitch-angle distribution of suprathermal-electron flux, proton density, bulk speed, proton temperature, total pressure in black (plasma thermal pressure in blue, magnetic pressure in red), the total field strength, the components of the magnetic-field vector in RTN coordinates, and the proton β. The RTN coordinate system is defined such that unit vector R points radially away from Sun to spacecraft, unit vector T is perpendicular to R and points in the direction of planetary motion, and vector N completes the right-handed system. At 12:00 UT on 21 January, the middle of the period considered, ST-B was at −69.92°, 0.29° in HEE longitude and latitude, respectively, at a heliospheric distance of 1.028 AU.

ST-B observed the interplanetary counterpart of the CME during 20 – 21 January 2010 as illustrated in Figure 14. According to the plasma and magnetic-field variations, we chose the boundaries of the ICME as delineated by the pair of vertical dashed lines. During this period, from 20 January 20:00 UT to 21 January 22:30 UT, the magnetic-field strength is enhanced, the proton temperature is low and the magnetic-field vector executes a large rotation. Thus, the configuration satisfies the magnetic cloud criteria (Burlaga *et al.*, 1981). From the North-to-South BN variation during eastward BT, the flux rope was right-handed.

The pitch-angle distribution of the suprathermal electrons from the IMPACT *Solar Wind Plasma Electron Analyzer* (SWEA: Sauvaud *et al.*, 2008), Figure 14 top panel, generally indicates an intense beam at low pitch angles, suggesting that the field lines were not connected back to the Sun at either end. There was about a five-hour period of bidirectional electron strahl in the leading part of the ICME up to ≈ 02:00 UT on 21 January, albeit with a much stronger intensity parallel to the field. Note from Figure 14 that this interval coincided with a very low proton density, a "ledge" of higher speeds and temperatures, and a very low proton β.

The MC was very slow [≈ 320 km s^{-1}] and did not drive any shocks observed *in situ* at 1 AU. There were no clear signatures of radial expansion, *i.e.* a monotonically decreasing V-profile. Instead, there was a slight increase in V up to 21 January ≈ 12:30 UT followed by a slow decrease. At 21 January ≈ 06:10 UT the T and N components of the magnetic field exhibited a sharp change at the same time as some of the other parameters also changed abruptly. We discuss this feature below in more detail. The enhancement of the proton number density at the central part of the ICME is not unusual, and is probably the remnant of the relatively dense ejecta that survived after the weak expansion. The proton temperature was not low in comparison with ambient solar wind, probably also related to the weak expansion. The temporal profile of the total pressure (the sum of plasma thermal pressure and magnetic pressure) had a central maximum. According to the definition of three groups of ICMEs by Jian *et al.* (2006), this event is a Group 2 ICME in which the pressure profile has a plateau.

4.2. Boundary Layers

There are transient signatures bracketed by two field and flow discontinuities where the field strength decreases strongly. These are most likely current sheets that are planar and have a

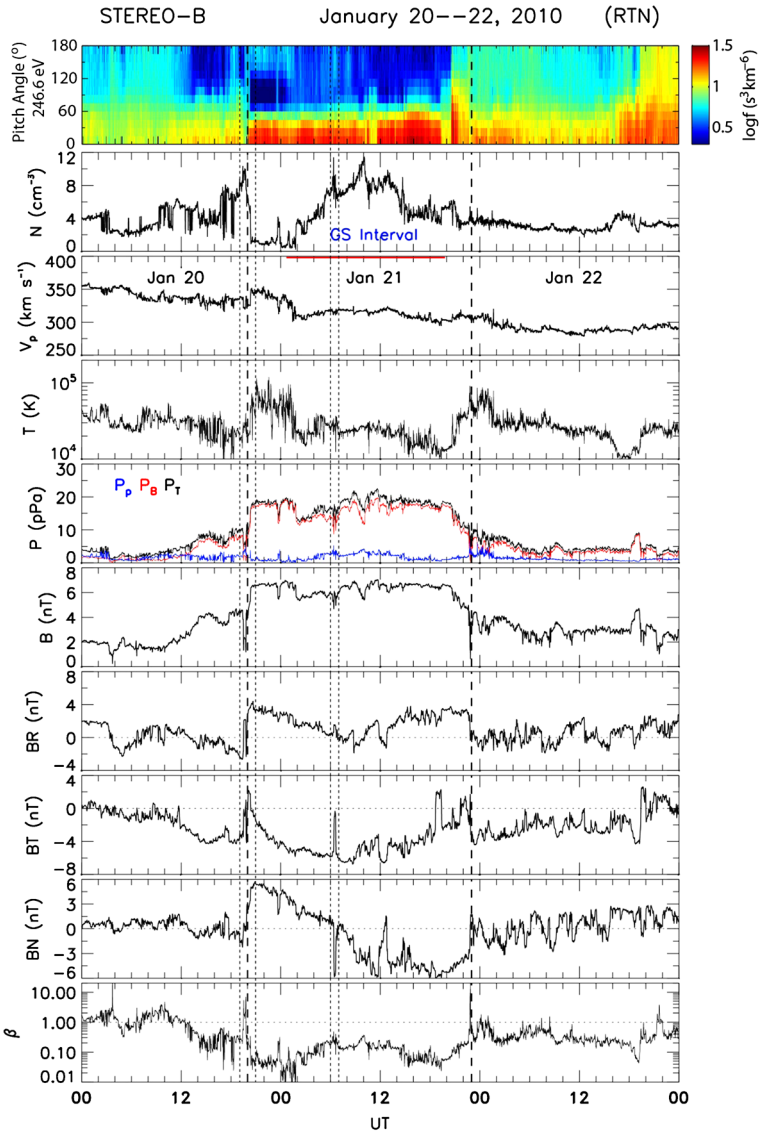

Figure 14 ST-B *in-situ* measurements of the ICME using data at one-minute resolution, except for the pitch-angle distribution data of suprathermal electrons, which is plotted with a 20-second resolution. From top to bottom: pitch-angle distribution of suprathermal electrons at the energy level of 246.6 eV; proton number density; proton bulk flow speed; proton temperature; the plasma thermal (blue), magnetic (red), and total (black) pressures; magnetic-field magnitude; magnetic-field vectors in RTN coordinates; and plasma β. The color scale in the first panel shows the logarithmic of the phase-space density. The vector is in RTN coordinates; R is the unit vector from the Sun to spacecraft; T is $(\Omega R)/|\Omega R|$ with Ω as the Sun's spin axis, and N completes the right-handed system. The bold vertical dashed lines bound the leading and trailing edges of the ICME. The pair of thin dashed lines denotes the boundary layers discussed in Section 4.2. The horizontal red bar at the bottom of the density panel labeled "GS interval" indicates the sub-boundaries within the ICME interval that were used for the G–S modeling (see Figure 19).

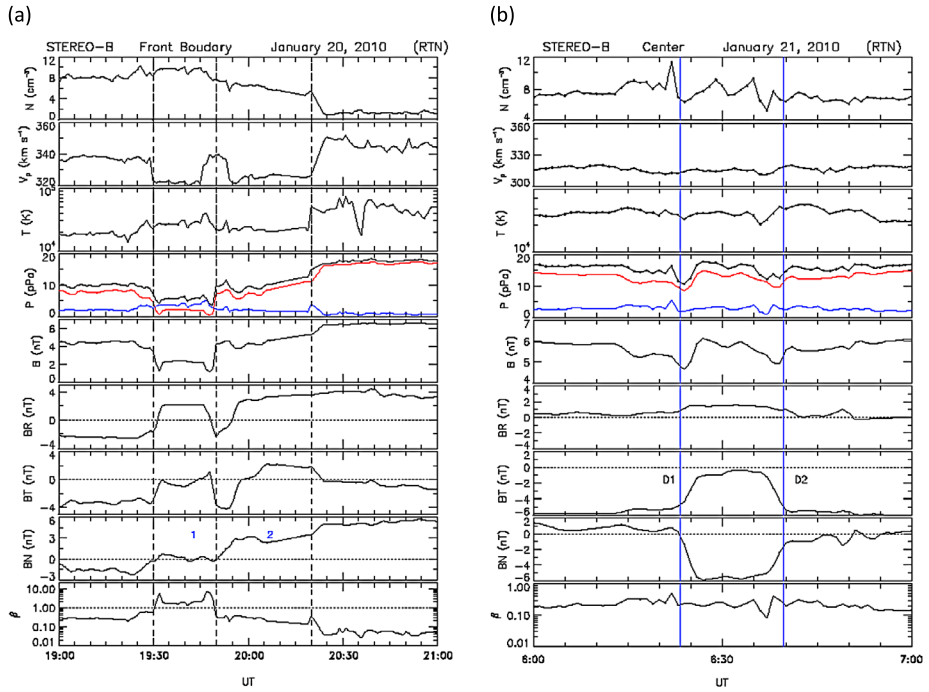

Figure 15 Expanded periods from the previous ST-B *in-situ* plot. (a) Temporal profiles of field and plasma variations in a two-hour region forming the front boundary of the transient. The three vertical lines indicate two contiguous intervals where a three-step variation (double bifurcation) can be seen. (b) A one-hour interval showing a double rotation of the magnetic-field vector.

twin-bifurcated (three-step) magnetic-field transition, suggestive of reconnection layers (not discussed further here, but see Gosling and Szabo, 2008). A clear tangential discontinuity is observed inside the transient, which, in turn, suggests a pair of transients. Both transients satisfy criteria for magnetic clouds with the geometry of a magnetic-flux rope. The normal to the front boundary of the structure is perpendicular to the axis of the first transient, as determined by minimum-variance analysis of the magnetic field data. A Grad–Shafranov fit to this structure is discussed in Section 4.3.3.

From Figure 14 it is clear that the transient interval starts at a field and flow discontinuity and the rear boundary at a field discontinuity. These two boundary-layer regions are denoted in Figure 14 by a pair of vertical dashed lines. We illustrate the nature of the first discontinuity in Figure 15a, which plots the same parameters as Figure 14, except that they are for the two-hour interval 20 January 19:00 – 21:00 UT. It is clear that the "discontinuity" really consists of a three-step rotation of the B-vector, and therefore it is more like a boundary layer. There are two clear depressions in the flow speed. The first (between the first two vertical guidelines) appears to be in approximate pressure balance (black trace in panel 4).

By carrying out a minimum-variance analysis on the magnetic-field data (Sonnerup and Cahill, 1967) for the interval 20 January 19:00 – 21:00 UT, we obtained a very robust planar structure. The ratio of intermediate-to-minimum eigenvalues is $\lambda = 9.7$. By a "robust" normal we mean, following Lepping and Behannon (1980) and Bothmer and Schwenn (1998), that the ratio exceeds two. The field-normal component $B_n = -0.87 \pm 0.42$ nT, which is

consistent with zero. Thus, all of the rotations occurred in a planar structure, the normal to which is $(-0.71, 0.57, 0.41)$.

Taking the whole period (20) 20:00 UT – (21) 22:30 UT, we derive a very good ($\lambda = 5.3$) result. Taking the intermediate vector (Goldstein, 1983), we obtain an axis direction of $(0.53, 0.84, -0.079)$ [RTN]. This axis is inclined at 85.7° to the normal to the planar structure that forms the front boundary.

We now focus on the feature at 21 January ≈6:30 UT. A one-hour period centered on this is given in Figure 15b. The rotation of the field occurs on 21 January 06:14 – 06:50 UT. It essentially consists of two successive discontinuities, labeled D1 and D2 in the figure. We examined this by minimum-variance analysis. For D1 the routine returned a robust normal with a ratio of intermediate-to-minimum eigenvalues $\lambda = 4.0$. The normal is $(0.74, 0.50, 0.45)$ and $B_n = -1.99 \pm 0.12$ nT, implying a rotational discontinuity. For D2, $\lambda = 2.2$. The normal is $(0.60, 0.49, 0.64)$ with $B_n = -2.93 \pm 0.18$ nT. The two normals subtend an angle of 13° to each other, so that we have two almost parallel directional discontinuities. Interestingly, the normal to the front boundary is practically perpendicular to D1 and D2. This suggests that the front boundary is almost perpendicular to the planes of D1 and D2. In summary, we have a configuration i) at whose front boundary signatures consistent with reconnection are present, and ii) that contains a sharp and large field rotation at its center. The orientations of the front boundary and the field discontinuities are consistent with the presence of two structures oriented parallel to each other. This is a typical signature of a reconnection exhaust in the solar wind, consisting of a bifurcated current sheet with correlated field and flow variations at one end and anticorrelated variations at the other.

4.3. Magnetic Cloud Measurements and Flux Rope Fits

Above we described the MC and its possible boundaries at ST-B observed from late 20 January through most of 21 January. In this section we describe independent flux-rope fits to the cloud made by several of the authors. Most of these models assume a cylindrical geometry with fixed quantities along the axis. Usually, specific assumptions are made, such as a force-free magnetic field and stationary or radial expansion in time. These models yield the basic parameters of the flux ropes, *e.g.* radius, axial magnetic field, and helical handedness. They can usually be compared only with data from single-spacecraft crossings, yielding measurements along a single radial line through the MC. Crossings of MCs by multiple spacecraft are rare.

It is generally acknowledged that the accuracy of model parameters decreases markedly with encounters farther from the MC axis and that the difficulty in accurately determining the boundaries of the flux rope can be a significant limitation (*e.g.* Al-Haddad *et al.*, 2013). Many simulated or fitted flux ropes have a simple geometry such as a circular or elliptical cross-section. But if the real cloud geometry is distorted by evolution through the solar corona or by dynamical interactions in the solar wind, the fitted parameters will be less reliable. Thus, even if the modeled profiles match the *in-situ* data well, the resulting parameters must be treated with caution. For this event we have addressed these problems by producing several independent fits or models of the MC and intercomparing the results. A total of four flux-rope fits were made, three assuming circular geometry, and one using the Grad–Shafranov (G–S) reconstruction technique. All of the models except the G–S model assumed that there was a single flux rope to be fitted. Essentially, the same ST-B-centered solar coordinate system was used for all the fits.

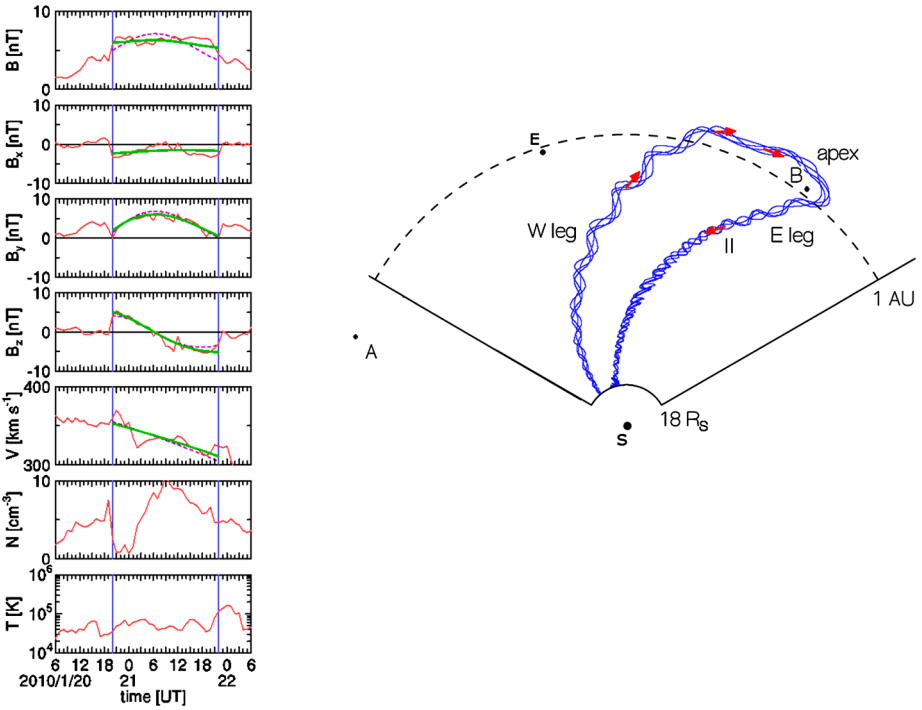

Figure 16 Flux-rope fits to MC observed at ST-B on 20 – 21 January 2010. (Left) ST-B *in-situ* data with MC boundaries marked by vertical blue lines. The plot displays from top to bottom the magnetic-field magnitude [B], the magnetic field components B_x, B_y, and B_z (in GSE), velocity [V], number density [N], and temperature [T]. The purple dashed line is the circular cylinder fit; the green line is the elliptical cylinder fit. (Right) Simulated flux rope lying in the Ecliptic plane, after its front has reached 1 AU and oriented to mimic this event. Thin helical lines in blue are magnetic-field lines of the flux rope. Parts of the flux rope are labeled as apex, W (west) leg, and E (east) leg. The dashed arc is the distance of 1 AU. Positions of ST-(A), (E)arth, ST-(B), and the (S)un are noted. After Vandas, Romashets, and Geranios (2010).

4.3.1. Circular and Elliptical Cylindrical Flux-Rope Fits

Coauthor Romashets and colleague M. Vandas produced flux-rope fits to the 20 – 21 January MC assuming both cylindrical and elliptical MC geometries. Their methods were discussed by Vandas, Romashets, and Geranios (2010) and earlier by Vandas and Romashets (2003) and Vandas, Romashets, and Watari (2005). In the left panel of Figure 16, the ST-B *in-situ* magnetic-field and plasma data are shown with the selected MC boundaries marked by vertical blue lines, *i.e.* 20:00 UT (20) – 22:00 UT (21). Note that these boundaries are nearly identical to those of the ICME defined in Figure 14 and include the "ledge" of higher plasma temperatures and velocities, but lower densities that are excluded in the G–S analysis below.

This flux-rope model assumes a constant-α, force-free magnetic structure inside a cylinder, either circular or elliptical, and includes radial expansion of the flux rope. The amount of expansion is estimated from the observed velocity profile. The orientation of the flux-rope axis is given by two angles: the inclination [θ_c] and the azimuthal angle [ϕ_c]. This is a generalization of the Lundquist solution, which is often used as a model for MC fitting (*e.g.* Burlaga, 1988; Lepping, Jones, and Burlaga, 1990). The generalization includes oblateness and expansion of the MC. The oblateness is conserved during expansion and incorporated by

Table 2 Flux-rope fit parameters from the cylinder and ellipse models (Section 4.3.1).

	Lat. [°]	Long. [°]	$R_\odot$ [AU]	P	Hand.	Axial B_0 [nT]
Cylinder	−7	68	0.1	0.52	RH	8.4
Ellipse	−5	59	0.15	0.7	RH	12.9

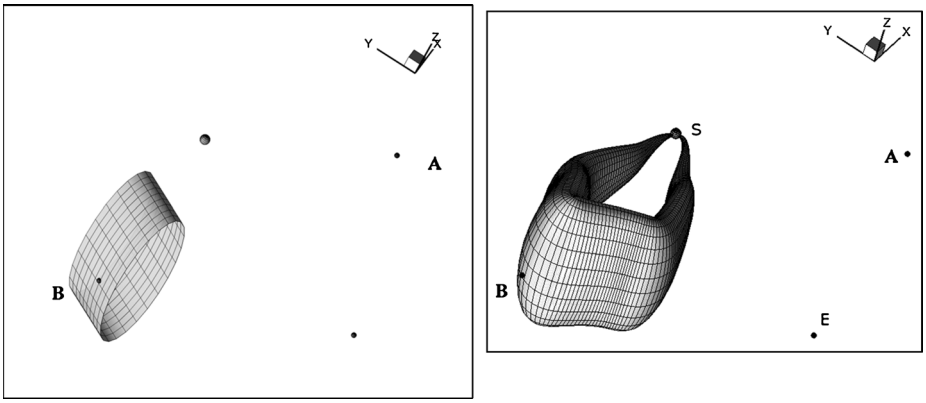

Figure 17 3D views of the structure and orientations of the Romashets and Vandas flux-rope fits. (Left) Local view of the elliptical cylinder fit. (Right) A possible global schematic view of the MC fitted by the elliptical solution with the MC legs extending back to the Sun. The result is derived from a 3D time-dependent MHD simulation with initial lower boundary condition in the form of half-toroid. The two fits are similar except that the elliptical fit provides a better match to the total B magnitude.

time-dependent and axial magnetic-field parameters. The coordinate system used is a rotated RTN system, with the x-, y-, and z-directions related to the RTN system as $x = -r$, $y = -t$, and $z = n$. Although strictly speaking, these systems are based on the solar equatorial plane, not on the ST-B centered solar Ecliptic coordinates used in Section 3, the differences are minor.

For this event the resulting fits are as follows: the purple dashed line in the plot is the result of the circular cylinder fit and the green solid line is the elliptical cylinder fit. The resulting flux-rope fit parameters for the circular-cylinder and elliptical-cylinder fits are given in Table 2, where *Lat.* is the inclination angle of the axis from the Ecliptic plane (northward positive), *Long.* is the azimuthal angle with the Sun–ST-B line of radius, R_0 is the radius, a and b are the major and minor radii of the ellipse, and p is the impact parameter. The impact parameter is given by the distance from the axis to the spacecraft trajectory, along the x-axis, at closest approach, normalized by r_0. This quantity is defined to be measured as the vector product of two vectors: one parallel to the x-axis, the other parallel to the cylinder axis.

The right panel of Figure 16 is a schematic view in the Ecliptic plane of the field lines of a simulated flux rope oriented to mimic this event when its front is crossing 1 AU. The locations of ST-A, Earth, ST-B, and the Sun are indicated. Figure 17 shows 3D views of the Romashets and Vandas elliptical flux-rope fits for the event. The cylindrical and elliptical fits are similar except that the elliptical fit better matches the observed total B. Note that the flux-rope orientations of these fits suggest that ST-B encountered the flux rope at its eastern edge, or leg, with fairly large impact parameters ≥ 0.5. Thus, the axis and most of the flux rope lay to the *West* of ST-B. One of the difficulties in interpretating the MC is

Table 3 Flux-rope fit parameters from the cylindrical model (Section 4.3.2).

	Lat. [°]	Long. [°]	$R_{\odot}$ [AU]	P	Hand.	Axial B_0 [nT]
Cylinder	−9.7	62	0.10	0.56	RH	9.6

that because its magnetic-field profile is not very pronounced, determining its parameters is more uncertain.

4.3.2. Cylindrical Flux-Rope Fit

Coauthor Marubashi provided a third flux-rope fit for this event. He used MC boundaries nearly identical to those of the ICME in Figure 14 and those of Romashets and Vandas, *i.e.* 20/21:00 UT – 21/22:00 UT. He used the constant-α, force-free model, including self-similar expansion, originally proposed by Farrugia *et al.* (1993). In this model, the flux-rope radius [r], the expansion velocity [v], and the magnetic field [B] at time t after the time of the first encounter with a spacecraft, were calculated using a time parameter [T_0] (see Marubashi and Lepping, 2007 for details).

The parameters of MCs to be determined by the model fitting are:

i) $U_{\rm sw}$ = the bulk-flow velocity of the solar wind, or the speed of the MC at the center. The solar-wind velocity variation within an MC is taken as the vector sum of $U_{\rm sw}$ and the expansion velocity $= (r/T_0)/(1 + t/T_0)$ (the direction is perpendicular to the cylinder axis).
ii) B_0 and R_0 = the magnitude of the magnetic field at the cylinder axis and the radius of the MC cylinder at time $t = 0$, as described above.
iii) θ_a, ϕ_a, and p are the latitude and longitude angles of the cylinder axis and the impact parameter, respectively. The latitude and longitude angles are given in the ST-B-centered rotated RTN coordinate system discussed earlier. The temporal variation of the distance between the spacecraft and axis is shown in the sixth panel of Figure 18 ($R_{\rm sat}$: AU).
iv) $E(T_0)$ = the expansion rate. In the self-similar expansion (Farrugia *et al.*, 1993), E is related to the time period [T_0] during which the flux-rope expansion had proceeded before the first encounter with the spacecraft as $E = 1/T_0$.
v) SGN = the sign of the magnetic-field-handedness of the MC.

The set of seven parameters listed in items i) – iv) determines the duration of the MC passage by the spacecraft. Because the durations of MCs are given by observations, it can be said that there is one relationship among the seven parameters. Figure 18 shows the results of this cylindrical flux-rope fit for the January event: (left) fit results superposed on the ST-B *in-situ* data, and (right) the 3D view. The RMS values at the bottom left are used to provide an error estimate of the fitting. RMS ($B_{\rm vec}$) = root mean squares of (observed $\boldsymbol{B}$ – calculated $\boldsymbol{B}$). The overall error is defined as the rms difference between the observed and calculated fields divided by the highest observed field intensity. A value < 0.3 is deemed acceptable.

The basic results are given in Table 3 and are very similar to either of the fits in Section 4.3.1. The flux-rope cylinder orientations are both West-to-East with a slight tilt out of the Ecliptic plane. In addition, the longitude of 62° suggests an ST-B crossing at the eastern side of the flux rope not too far from the center. Thus, most of the flux rope passed to the *West* of ST-B.

Marubashi also provided a torus flux-rope fit for the 20 – 21 January event, but the resulting MC orientation was very different from the cylinder results. This torus model is

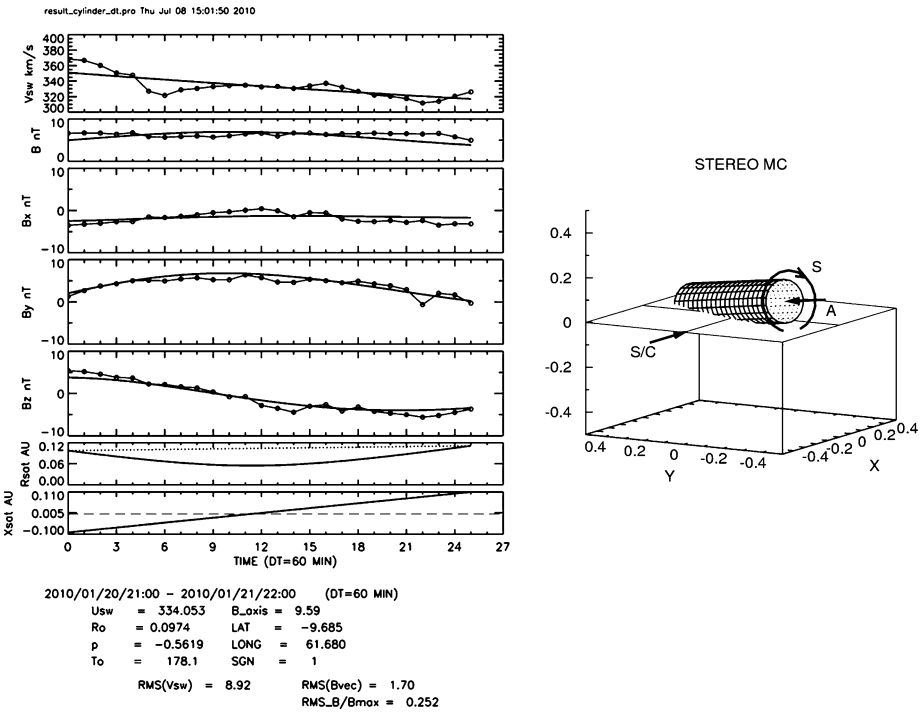

Figure 18 Cylindrical flux-rope fit of Marubashi. *In-situ* (left) and 3D view (right in AU units) of the circular cylindrical flux-rope fit for the January event. This fit is very similar to either of the Romashets and Vandas fits. The cylinder orientation was West-to-East with a slight tilt out of the Ecliptic plane.

the simplest approximation of the curved portion of the flux-rope loop and was applied only where the spacecraft traversed near the flank of the loop (Marubashi and Lepping, 2007). The torus plane (that of the MC loop) was mostly perpendicular to the Ecliptic plane, whereas the cylinder fits were nearly parallel to the Ecliptic. To agree with the solar data, therefore, we would have to assume a $\approx 90^\circ$ rotation of the MC during its passage to 1 AU. Although the magnetic-field variation in the January MC could be reproduced by a torus fit just as well as the cylinder fit, its geometry was not consistent with other analysis results. Thus, we did not consider the torus model further (see Marubashi and Lepping, 2007 for some detailed comparisons between torus- and cylinder-model fitting).

4.3.3. Grad–Shafranov MC Reconstruction

As discussed in Section 4.2, a clear tangential discontinuity was observed inside the transient, which, in turn, suggests a pair of transients. Both transients satisfy criteria for magnetic clouds with the geometry of a magnetic-flux rope. We analyzed these transients as discussed in this section. The normal to the front boundary to the structure was perpendicular to the axis of the first transient, as determined by minimum-variance analysis of the magnetic-field data. The G–S reconstruction was then applied to a region smaller than the observations.

The G–S method is applicable to systems in magnetohydrostatic equilibrium and that possess an invariant direction (an axis; taken here along z'). MCs in the solar wind satisfy these criteria – at least locally, around the position of a spacecraft, and if the expansion of

the MC is negligible as it passes the spacecraft. We used this method on the 20 – 21 January MC in a similar way to Hu and Sonnerup (2002), who first applied the technique to MCs. For simplicity, we refer for details and equations to that original article. Briefly, the MC field lines are reconstructed in a frame co-moving with the cloud with constant velocity [$\boldsymbol{V}_{\rm HT}$], the so-called deHoffmann–Teller frame (Khrabrov and Sonnerup, 1998). To find the correct orientation of the MC axis, the technique uses the fact that the pressure transverse to the invariant direction [Pt], which is a function of the vector potential [$\boldsymbol{A}$], must be single-valued along a spacecraft trajectory, as it travels into the MC and outward again (see Hu and Sonnerup, 2002 and Möstl *et al.*, 2009 for details). The result of the analysis is shown in Figure 19a. The solid and dashed black function is a fit to observed values of $P_t(A)$. The residual $R_f = 0.07$ indicates that a very good fit has been found. The magnetic-field data were then re-sampled to 15 points using a running average. We then recovered a 2.5D cross-section of the transient in a plane perpendicular to the axis by integrating away from the spacecraft trajectory. These were used as initial values to solve the Grad–Shafranov equation, which was used for the previously mentioned integration. In carrying out the G–S analysis and by omitting the "ledge" mentioned above, we used a shorter 19-hour interval, 21 January 00:41–19:51 UT, indicated by the red horizontal bar below "GS interval" in Figure 14.

Figure 19b shows contour lines of the reconstructed magnetic field in the plane perpendicular to the invariant axis, which is pointing out of the plane of the figure. The color refers to the strength of the component along the axis [B_z']. The heavy white trace gives the boundary of integration, associated with value A_b of the vector potential (solid vertical line in Figure 19a). Note that in the figure, the Sun is to the right and the MC propagates to the left. However, because the axial field points to solar East, the direction of solar North is roughly to the bottom of the figure, and the top of the figure roughly points toward solar South. Clearly, the technique yields two distinct flux ropes that, however, seem to be in the process of coalescing. This conclusion supports the general indications discussed earlier, and similar double-rope G–S results were found by, *e.g.*, Hu *et al.* (2004). By construction, the two flux ropes have a common orientation. The cross-section of each flux tube is almost circular. In RTN coordinates the orientation is $z = (-0.4204, -0.8106, -0.3914)$; θ (latitude as inclination to RT plane [$=0°$]) $= -23°$; ϕ (longitude as measured from $\boldsymbol{R}$ (0°) to $\boldsymbol{T}$ (90°) $= 243°$. In the GSE system, the longitude angle ϕ is approximately 63°. The accuracy of these values is estimated to be $\pm$ 10°. The cloud is an NES-type ($+\boldsymbol{N}$, $-\boldsymbol{T}$, $-\boldsymbol{N}$), so the axis is pointing roughly along $-\boldsymbol{T}$, or solar East. Other quantities are derived and shown in Table 4. The scale size along the spacecraft trajectory is 0.139 AU. Both flux ropes are right-handed. The impact parameter, *i.e.* the closest approach to the axis, is 0.21, normalized to the scale-size along the spacecraft trajectory. The flux-rope axis from the G–S analysis at ST-B is tilted so that the axis points along a direction approximately between $-T$ and $-R$, if one looks down onto the solar equatorial plane. If the MC is a tube extending from the Sun, the apex of that tube would be *West* of ST-B. This direction is consistent with the results from the other flux-rope fits in Sections 4.3.1 and 4.3.2 (see also Figures 16 and 17).

Two very important quantities, also given in Table 4, are the poloidal [ϕ_p] and the toroidal [ϕ_t, *i.e.* axial] fluxes (see Qiu *et al.*, 2007 for definitions how to obtain them from the G–S technique). These are useful for comparison with a putative solar source, as has been shown in various articles (*e.g.* Qiu *et al.*, 2007; Möstl *et al.*, 2009). We obtain 0.14×10^{21} Mx and 0.32×10^{21} Mx for the axial and poloidal fluxes, respectively. For the poloidal flux, the length of the flux tube is an unknown for which we assumed a value of 1 AU.

We set these numbers into context by considering the fluxes for MCs analyzed by Qiu *et al.* (2007), who considered a sample of MCs with a wide range of fluxes. The poloidal

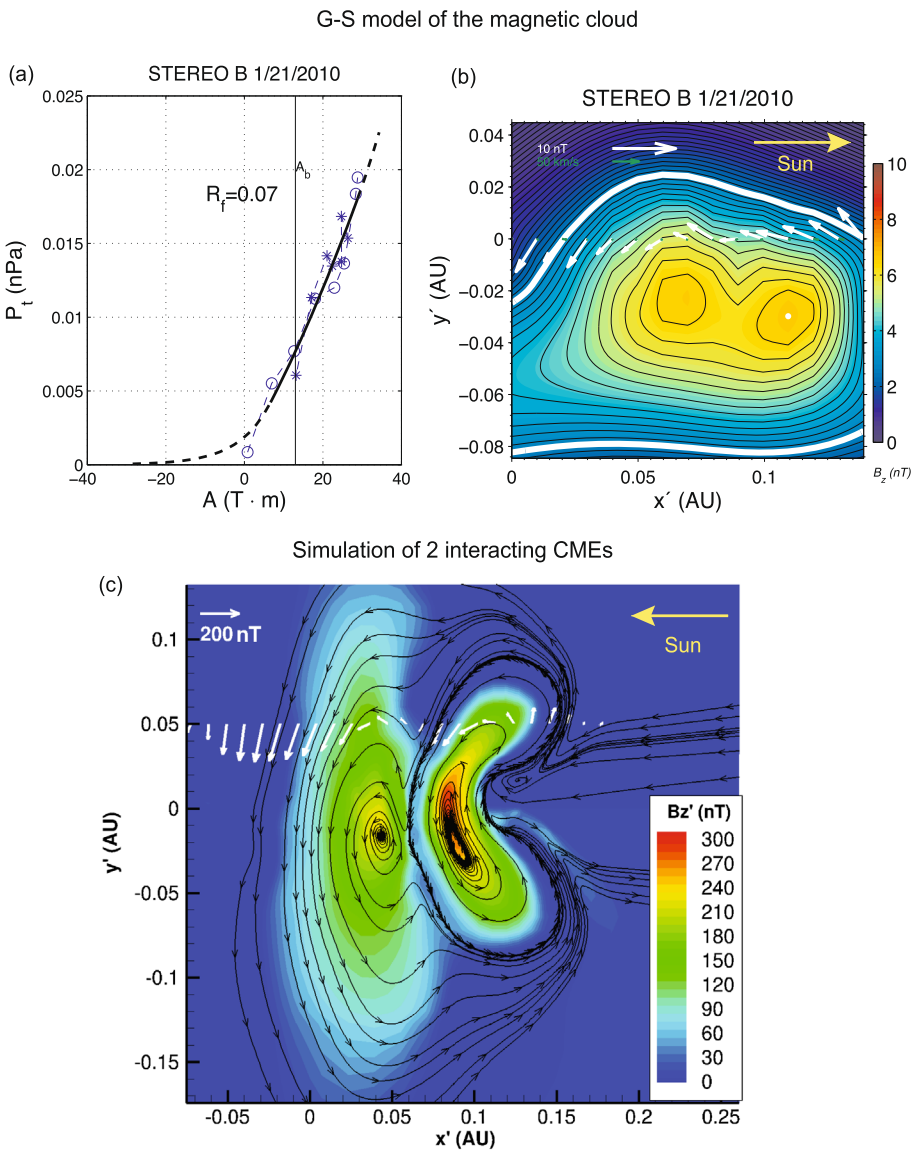

Figure 19 Grad–Shafranov modeling of the magnetic cloud cross-section, and comparison with a numerical simulation. (a) A fit (solid and dashed black) to the transverse pressure [P_t] as a function of the magnitude of the vector potential [$\boldsymbol{A}$]. Observations are shown by circles (first half of the flux rope) and stars (second half). This illustrates that an invariant axis has been successfully found by the method. (b) The resulting magnetic configuration of a double flux rope. The MC front boundary is to the left side of the figure and the Sun is to the right, as shown. The magnetic-field orthogonal to the axis, which is pointing out of the plane, is shown by black contour lines. The color code gives the strength of the axial field. The thick white curve gives the MC boundary. The handedness and orientation of the two flux ropes are consistent with the other MC modeling results. (c) Results of an MHD simulation of two interacting CMEs 20 hours after the initiation of the first CME showing the axial magnetic field [B_z'] color-coded and 2D projection of magnetic-field lines in black. The x'-axis is shifted and the origin corresponds to a radial distance of 0.23 AU with the Sun toward the left. The Earth is on the right-hand side and solar North is at the bottom.

Table 4 Physical quantities resulting from the Grad–Shafranov reconstruction (Section 4.3.3).

Axial $B_{\max}$	Orientation $[\theta, \phi]$ [GSE]	Handedness	Size along s/c traj.	P^1	Φ_t	$\Phi_p \times 10^{21}$ Mx	Axial I_t^2
6.8 nT	−23°, 63°	RH	0.139 AU	0.21	0.14	0.32	207 MA

[1] = impact parameter normalized to the scale size along the spacecraft trajectory;

[2] = the axial current.

flux for the 20 – 21 January event is at the lower end of their distribution, consistent with the weaker magnetic-field strength. Qiu *et al.* (2007) also stated a relationship between the axial and poloidal MC flux: $\phi_t = a\phi_p^{1.32}$, with $a = 0.32$, established by using a variety of techniques. Using the numbers for the 20 – 21 January MC, and solving for the factor a, gives $a = 0.63$. Thus, the axial flux is clearly enhanced in the present event by about a factor of two compared with average MCs, which could be a consequence of the coalescing flux ropes.

We do not have a good explanation for the coalescing, two-flux-rope structure observed in this MC. Although such a structure could arise from the interaction of two CMEs (Figure 19c), the presence of two interacting CMEs is not consistent with the coronagraph and HI imagery discussed in Section 3. Figure 19c shows the results of an MHD simulation of such an interaction between two CMEs using the Space Weather Modeling Framework (Tóth *et al.*, 2012), and demonstrates qualitative agreement between Figures 19b and 19c. The selected parameters are very similar to the simulation of Lugaz, Manchester, and Gombosi (2005): two CMEs with the same orientation and helicity sign and launched from the same location on the solar disk using a Gibson–Low flux rope (Gibson and Low, 1998). They are both of the NES type, the same orientation as that of the event in January 2010. Figure 19c shows the magnetic field of the compound event 20 hours after the initiation of the first CME at a time when the front of the first magnetic ejecta is at 0.35 AU. The simulation results are shown in a style similar to that of the G–S reconstruction for easy comparison. The magnetic-field vector along an artificial-satellite track through the event is shown with white arrows, for a positive impact parameter.

5. Summary and Discussion

5.1. Overview

We analyzed the development and propagation of a slow CME that was aimed toward ST-B and probably was the source of an ICME/MC appearing six days later at ST-B. Coronal imaging from the SECCHI-EUVI and COR and SOHO/LASCO telescopes and heliospheric imaging from the SMEI and SECCHI-HI instruments permitted tracking of the dense material during this period through the heliosphere to 1 AU, confirming that the 14 – 15 January 2010 solar event was the source of the 20 – 21 January ICME/MC. The late-14 January CME was associated with a filament eruption and arcade that crossed the central meridian, was a halo CME from COR2-B, and could be tracked to 1 AU with SMEI and STEREO imaging, with its travel time and speed matching the arrival time and speed of the MC at ST-B. We used several empirical models to understand the 3D geometry and propagation of the CME, analyzed the *in-situ* characteristics of the associated ICME, and investigated the characteristics of the MC by intercomparing four independent flux-rope model fits. We examined

spacecraft *in-situ* data from ST-B at 1 AU, *Wind*, and ACE at the Sun–Earth L_1 point, and MESSENGER, which lagged Mercury in its orbit.

The energetic 17 January CME was initially considered the progenitor of the ST-B MC because of the reasonable three- to four-day travel time, the partial halo views from LASCO and COR2-A, the relatively low level of preceding solar activity, and the isolation of the cloud. However, once we connected the 14 – 15 January CME and 20 – 21 January ICME, it remained a puzzle why we could not identify and track the material from the 17 January CME in the SMEI and HI FoV. The LASCO and COR2-A coronagraphs revealed the CME as a partial halo extending over the South Pole. We now think it likely that these were backside views of the CME moving away from these two spacecraft. Considering this, it is therefore likely that the CME propagated too far around in longitude for the SECCHI HIs to view it (Figures 1b and 9b), and was within the SMEI zone-of avoidance to the east (Figure 5a).

5.2. Comparisons of 3D Heliospheric Modeling

In Section 3 three different sets of coronagraph and heliospheric imaging data were used to produce 3D reconstructions of the geometry and propagation of the 14 – 15 January event. We were careful to ensure that these three analyses were performed independently by the different coauthors, who did not know of the others' results until they were completed.

Coronagraph data alone were used to determine the CME's near-Sun geometry, direction of propagation, speed, dimensions, and mass using a combination of four independent techniques (Section 3.3): geometric localization, polarimetric localization, mass independence on viewing perspective, and a three-view reconstruction technique (CARP). The derived parameters were consistent with those from the HI results and the *in-situ* measurements. For example, the derived speed of 310 ± 20 km s^{-1} is consistent with the speed used in the HI reconstructions to match the average speed in the MC of 320 km s^{-1}. In addition, assuming the CME was a planar structure and that its total mass was independent of observer viewpoint, the COR2 images were used to estimate the CME direction of propagation as well as its corrected mass, 3.8×10^{15} grams. This mass is similar to that determined for LASCO-C2.

The SMEI (Section 3.1) and SECCHI-COR and -HI (Section 3.2) data were used to derive the geometry, size, and propagation characteristics of the CME/ICME in the heliosphere from independent 3D reconstruction techniques. For SMEI, the UCSD CAT technique was used to produce 3D reconstructed volumes and fish-eye, Ecliptic, meridional, and remote observer views of the inner heliosphere encompassing the time period of the 14 – 21 January CME passage (Figures 4 – 7). The reconstructed and *in-situ* densities were found to correlate well (Figure 8). In Section 3.2 a well-developed empirical kinematical modeling technique was used to propagate a morphological reconstruction of the CME to 1 AU. As with SMEI, the arrival time at ST-B was well matched, but the duration of passage was two days instead of the $\approx$ one day *in-situ* duration. Different thicknesses of the modeled flux rope will yield different durations.

The heliospheric results from these two 3D reconstruction techniques are quite consistent with each other. The Ecliptic-plane views (Figures 5a and 9b) and the model flux rope (Figure 10b) show a flattened, extended front at 1 AU and that ST-B encountered the ICME near its western side, *i.e.* most of the ICME material passed *east* of ST-B. These observations and 3D reconstructions of the heliospheric material demonstrate how unique and essential such data are for the identification and tracking of the dense material in solar transients. Such heliospheric imaging has also been shown to be essential to improved space-weather forecasting (*e.g.* Davis *et al.*, 2009; Howard and Tappin, 2010; Harrison *et al.*, 2012; Howard *et al.*, 2013).

The coronagraph results near the Sun are also mostly consistent with the heliospheric results. The ST-B, LASCO, and ST-A coronagraph observations suggest that the CME was launched along the solar equatorial axis, although it was tilted slightly North of the equatorial plane (Figure 3a). The heliospheric results indicate that the ICME was very planar and elongated, with its densest portion lying in or near the Ecliptic plane. All of this suggests that the front was highly flattened and that ST-B passed through the western side of the ICME-MC, *i.e.* most of the ICME material passed *East* of ST-B. It is remarkable that the results of all three methods independently yielded the same width of 55° for the ICME.

The results suggest that the major (longitudinal) axis of the structure was slightly tilted with respect to the Ecliptic plane. From both the 3D and multiple-method reconstructions we derived a tilt angle of about 5°. However, these were in opposite directions: viewed toward the Sun, the flux-rope method had the west side of the ICME tilted 5° above the Ecliptic plane, whereas the multiple method had the eastern leg tilted upward by 5°. However, this was a small rotation, and since the accuracy of these methods is considered no better than $\pm 5°$, it is not a robust result. On the other hand, it is interesting that, as we will see, all of the *in-situ* flux-rope fits also yielded an approximate 5° tilt.

The kinematic inputs to the SMEI and SECCHI heliospheric reconstructions used the *in-situ* speed measured in the ST-B MC and assumed that the propagation speed was constant with no acceleration or deceleration. Thus, their derived arrival times of the ICME at ST-B were consistent with the actual arrival time late on 20 January. Independently, the same CME speed near the Sun was derived by the coronagraph method, which also confirmed that the speed was constant from the Sun to ST-B.

5.3. Comparisons of *In-situ* MC Modeling

The ICME/MC was observed at ST-B $\approx$ six days after the launch of the CME on 14 – 15 January. In Section 4 the *in-situ* results at ST-B were discussed, including a summary of the ICME/MC characteristics, a discussion of boundary layers within the ICME, and the flux-rope model fits. During the ICME period, the magnetic-field strength was enhanced, the proton temperature was low, and the magnetic field showed a large rotation, thus satisfying the criteria of an MC. There was a $\approx$ five-hour period of bidirectional electron strahl in the leading part of the ICME, but later an intense beam at low pitch angles suggested field lines not closed at the Sun. The MC was very slow, ≈ 320 km s^{-1}, did not drive any shocks at 1 AU, and was not radially expanding. The proton density was enhanced at the center of the ICME, probably due to the relatively dense ejecta surviving the weak expansion. That the *in-situ* density peaked in the middle of the magnetic enhancement means that the enhanced densities of the heliospheric reconstructions should have been co-aligned with the MC at 1 AU. The proton temperature was not low in comparison with ambient solar wind, probably also related to the weak expansion.

Four independent flux-rope fits to the MC at ST-B were performed. Sections 4.3.1 and 4.3.2 described typical force-free models that assumed circular geometry with constant quantities along the axis. Section 4.3.1 involved circular cylindrical and circular elliptical fits, and Section 4.3.2 a circular cylindrical model fit. In Section 4.3.3 the Grad–Shafranov (G–S) reconstruction technique was used to model the MC. Essentially the same ST-B-centered solar coordinate system was used for all of the fits. All of these models yielded the basic parameters of the flux ropes, such as direction, radius, axial magnetic field, and handedness. It is well-known that the accuracy of model-fit parameters can decrease with encounters farther from the MC axis, the so-called impact parameter [P]. For the fits to this MC, P varied from 0.21 to 0.7. An accurate determination of the flux-rope boundaries

can also be a significant factor in the fitting. The circular fits assumed essentially the same boundaries, whereas the G–S model used narrower boundaries (Figure 14).

Because the MC was fairly simple, the size and orientations from the fits were consistent with each other. Tables 2, 3, and 4 show that the flux-rope radius was 0.1 – 0.15 AU, and the axial-orientation Ecliptic latitude values ranged from −5° to −23°, the longitudes from 59° to 68°. The helical orientation was right-handed for all of the fits. The flux-rope axis resulting from the G–S analysis was tilted and, if one assumes that the MC was a tube extending from the Sun, its apex would have been West of ST-B. Thus, for all of the MC fits, the main axis of the flux rope passed *West* of ST-B, *i.e.* in the direction toward Earth.

All of the flux-rope fits are consistent with the observed East–West launch orientation of the CME near the Sun, generally in the Ecliptic plane with a slight tilt out of that plane. The circular and elliptical fits and the G–S model also give similar results, including the fit to the total-B curve, which had a measured peak flux of 6.9 nT. The cylindrical fits gave ≈ 7 nT for the peak flux and the G–S model 6.8 nT. Our results are consistent with a few others that used similar force-free, elliptical, and G–S models, *e.g.* Riley *et al.* (2004) and Al-Haddad *et al.* (2013). In these two studies, the chosen boundaries were found to be important, and the magnitude of the axial field was consistent for all models, but the orientation showed large variations.

The G–S MC fit revealed evidence of a double structure; one interpretation for this is two distinct flux ropes that were in the process of coalescing. Such double structures have been observed before in MC fits and simulated, such as in the MHD-modeled interaction of two CMEs erupting seven hours apart shown in Figure 19c. However, we found no evidence for more than a single eruption at the Sun, for multiple structures during the propagation of the CME towards ST-B, or for multiple flux ropes in the cylindrical fits. Although the G–S fit impact parameter was relatively large, meaning that the spacecraft did not pass close to the cores, the G–S fit was good and revealed definite substructure in the magnetic-field data, as noted in Section 4. We note that the G–S method does not prescribe the number of flux tubes observed *in situ*; it could be one, two, three, or more. The number of tubes derived from G–S reconstruction is a result of the data convolved with the method, not an assumption, and it reveals that the MC structure was more complicated than that of a single flux tube. In contrast, the reason why other models do not obtain double tubes is that they would have to prescribe them manually; since they prescribed one tube, they obtained a one-tube reconstruction. Finally, our results again confirm multiple-event studies such as those of Riley *et al.* (2004) and Al-Haddad *et al.* (2013): single-point *in-situ* measurements can yield ambiguous results when modeling large-scale 3D structures.

In summary, ours is a detailed analysis of the propagation of a slow CME from its origin as a filament eruption/arcade at the Sun through the heliosphere to 1 AU, where it appeared *in situ* as an ICME containing a distinct MC. The CME had a nearly constant velocity over its ≈ six-day travel time. The heliospheric-density reconstructions were consistent with each other, revealing a flattened-front structure stretching 55° in longitude and lying mostly in the Ecliptic plane with a slight tilt out of the plane. The reconstructions show that ST-B passed through the western side of the ICME so that most of the ICME material passed *East* of ST-B.

The ST-B *in-situ* data revealed a slow ICME with no leading shock wave but containing a classic, but weaker MC of about one day duration. Several fits to the data suggest one (possibly two) flux rope with the axis lying nearly in the Ecliptic with a slight tilt, consistent with the density results. However, these fits placed the main axis of the flux rope to the *West* of ST-B, or in the direction toward Earth and opposite in longitude to the 3D-density reconstructions. Moreover, although all of the models found a small, ≈ 5°, tilt of the ICME/flux-rope axis out of the Ecliptic plane, the direction of the tilt was not the same among the

models. These discrepancies could arise because the 3D reconstructions reveal the overall density envelope of the ICME, whereas the *in-situ* fits are of the magnetic structure at only a single point. In addition, we might expect the CME density structure to be much wider than its flux rope, as is usually the case in MHD simulations. The tilt-angle discrepancies might be related to the uncertainties in the results, which are considered $\pm 5-10^{\circ}$ in each case.

These observations and 3D reconstructions of the heliospheric material demonstrate how unique and essential such data are for identifying and tracking the denser-than-ambient material in solar transients. We emphasize the crucial importance of using both observations and models to better understand the structure and propagation of CMEs. For example, in this case we were able to conclude that this weak eruption was the source of the MC only because we could track the CME from the low corona to 1 AU to establish the connection between the CME and its ICME/MC. The geometry and orientations of the CME from the heliospheric-density reconstructions and the *in-situ* modeling are remarkably consistent.

Heliospheric imagers have proven to be an important resource for both the scientific and the operational communities, with high-resolution imaging essential to improved space-weather forecasting. With the termination of the SMEI mission and with the STEREO spacecraft aging and now approaching solar opposition relative to Earth, future heliospheric imaging missions are vital to continue to develop and utilize this unique resource.

Acknowledgements We thank the Institute of Physics, University of Graz, Austria for hosting a workshop on this event in March 2011. We are grateful to the STEREO/SECCHI PI, Russell Howard, the STEREO/PLASTIC PI, Antoine Galvin, and the STEREO/IMPACT PI, Janet Luhmann, for the use of data and analyses from these instrument suites. We thank Gemma Attrill, John Clover, Timothy Howard, Nariaki Nitta, Dusan Odstrcil, S. James Tappin, and Marek Vandas for their analysis efforts on these events during the January 2010 period. The SMEI instrument is a collaborative project of the US Air Force Research Laboratory, NASA, the University of California at San Diego, the University of Birmingham, UK, Boston College, and Boston University. The STEREO/SECCHI *Heliospheric Imager* (HI) instrument was developed by a collaboration that included the Rutherford Appleton Laboratory and the University of Birmingham, both in the United Kingdom, the Centre Spatial de Liège (CSL), Belgium, and the US Naval Research Laboratory (NRL), Washington DC, USA. The SECCHI project is an international consortium of the Naval Research Laboratory, Lockheed Martin Solar and Astrophysics Lab, NASA Goddard Space Flight Center, Rutherford Appleton Laboratory, University of Birmingham, Max-Planck-Institut für Sonnensystemforschung, Centre Spatial de Liège, Institut d'Optique Théorique et Appliquée, and Institut d'Astrophysique Spatiale. We also benefitted from data from the SOHO mission, which is an international collaboration between and ESA and NASA, and also from the SOHO/LASCO CME catalog, generated and maintained by the Center for Solar Physics and Space Weather, The Catholic University of America in cooperation with NRL and NASA. The work of DFW was supported at Boston College by Air Force contracts AF19628-00-K-0073 and FA8718-04-C-0006 and Navy contracts N00173-07-1-G016 and N00173-10-1-G001. The work of CM was supported by the European Union Seventh Framework Programme (FP7/2007-2013) under grant agreement no. 263252 (COMESEP), and by a Marie Curie International Outgoing Fellowship within the 7th European Community Framework Programme. BVJ and H-SY were supported by UCSD NSF grant and AG-S-1053766, NASA grant NNX11AB50G, and AFOSR grant 11NE043. LKJ was supported by NSF grant AG-S-1242798 and by NASA's Science Mission Directorate as part of the STEREO project, including the IMPACT and PLASTIC investigations. MMB acknowledges support on these analyses initially from UCSD NSF grant ATM-0925023, and also from STFC funding to RAL Space at The Rutherford Appleton Laboratory. CJF was supported by NASA grant NNX13AP39G and NSF grant AG-S–1140211. Part of this work was supported by NASA (NAS5-00132) for STEREO/PLASTIC at UNH. CADK was supported by NASA TR&T grant NNX09AJ84G.

References

Al-Haddad, N., Nieves-Chinchilla, T., Savani, N.P., Möstl, C., Marubashi, K., Hidalgo, M.A., Roussev, I.I., Poedts, S., Farrugia, C.J.: 2013, Magnetic field configuration models and reconstruction methods for interplanetary coronal mass ejections. *Solar Phys.* **284**, 129. DOI.

Anderson, B.J., Acuña, M.H., Lohr, D.A., Scheifele, J., Raval, A., Korth, H., Slavin, J.A.: 2007, The magnetometer instrument on MESSENGER. *Space Sci. Rev.* **131**, 417.

Bisi, M.M., Jackson, B.V., Hick, P.P., Buffington, A., Odstrcil, D., Clover, J.M.: 2008, Three-dimensional reconstructions of the early November 2004 coordinated data analysis workshop geomagnetic storms: analyses of STELab IPS speed and SMEI density data. *J. Geophys. Res.* **113**, A00A11. DOI.

Bothmer, V., Schwenn, R.: 1998, The structure and origin of magnetic clouds in the solar wind. *Ann. Geophys.* **16**, 1.

Brueckner, G.E., Howard, R.A., Koomen, M.J., Korendyke, C.M., Michels, D.J., Moses, J.D., *et al.*: 1995, The large angle spectroscopic coronagraph (LASCO). *Solar Phys.* **162**, 357. DOI.

Burlaga, L.F.: 1988, Magnetic clouds and force-free fields with constant alpha. *J. Geophys. Res.* **93**, 7217.

Burlaga, L.F., Sittler, E., Mariani, F., Schwenn, R.: 1981, Magnetic loop behind an interplanetary shock: Voyager, Helios, and IMP 8 observations. *J. Geophys. Res.* **86**, 6673.

Chen, J., Howard, R.A., Brueckner, G.E., Santoro, R., Krall, J., Paswaters, S.E., *et al.*: 1997, Evidence of an erupting magnetic flux rope: LASCO coronal mass ejection of 1997 April 13. *Astrophys. J. Lett.* **490**, L191.

Colaninno, R.C., Vourlidas, A.: 2009, First determination of the true mass of coronal mass ejections: a novel approach to using the two STEREO viewpoints. *Astrophys. J.* **698**, 852. DOI.

Cremades, H., Bothmer, V.: 2004, On the three-dimensional configuration of coronal mass ejections. *Astron. Astrophys.* **442**, 307.

Davies, J.A., Harrison, R.A., Rouillard, A.P., Sheeley, N.R., Perry, C.H., Bewsher, D., *et al.*: 2009, A synoptic view of solar transient evolution in the inner heliosphere using the heliospheric imagers on STEREO. *Geophys. Res. Lett.* **36**, L02102. DOI.

Davis, C.J., Davies, J.A., Lockwood, M., Rouillard, A.P., Eyles, C.J., Harrison, R.A.: 2009, Stereoscopic imaging of an Earth-impacting solar coronal mass ejection: a major milestone for the STEREO mission. *Geophys. Res. Lett.* **36**, L08102.

de Koning, C.A., Pizzo, V.J.: 2011, Polarimetric localization: a new tool for calculating the CME speed and direction of propagation in near-real time. *Space Weather* **9**, S03001. DOI.

de Koning, C.A., Pizzo, V.J., Biesecker, D.A.: 2009, Geometric localization of CMEs in 3D space using STEREO beacon data: first results. *Solar Phys.* **256**, 167. DOI.

Delaboudinière, J.P., Artzner, G.E., Brunaud, J., Gabriel, A.H., Hochedez, J.F., Millier, F., *et al.*: 1995, EIT: extreme-ultraviolet imaging telescope for the SoHO mission. *Solar Phys.* **162**, 291. DOI.

Domingo, V., Fleck, B., Poland, A.I.: 1995, The SOHO mission: an overview. *Solar Phys.* **162**, 1. DOI.

Domingue, D.L., Russell, C.T. (eds.): 2007, The MESSENGER mission to Mercury. *Space Sci. Rev.* **131**, 1. DOI.

Eyles, C.J., Simnett, G.M., Cooke, M.P., Jackson, B.V., Buffington, A., Hick, P.P., Waltham, N.R., King, J.M., Anderson, P.A., Holladay, P.E.: 2003, The solar mass ejection imager (SMEI). *Solar Phys.* **217**, 319. DOI.

Eyles, C.J., Harrison, R.A., Davis, C.J., Waltham, N.R., Shaughnessy, B.M., Mapson-Menard, H.C.A., *et al.*: 2009, The heliospheric imagers onboard the STEREO mission. *Solar Phys.* **254**, 387. DOI.

Farrugia, C.J., Burlaga, L.F., Osherovich, V.A., Richardson, I.G., Freeman, M.P., Lepping, R.P., Lazarus, A.J.: 1993, A study of an expanding interplanetary magnetic cloud and its interaction with the Earth's magnetosphere: the interplanetary aspect. *J. Geophys. Res.* **98**, 7621.

Galvin, A.B., Kistler, L.M., Popecki, M.A., Farrugia, C.J., Simunac, K.D.C., Ellis, L., *et al.*: 2008, The plasma and suprathermal ion composition (PLASTIC) investigation on the STEREO observatories. *Space Sci. Rev.* **136**, 437.

Gibson, S.E., Low, B.C.: 1998, A time-dependent three-dimensional magnetohydrodynamic model of the coronal mass ejection. *Astrophys. J.* **493**, 460. DOI.

Goldstein, H.: 1983, On the field configuration in magnetic clouds. In: Neugebauer, M. (ed.) *Solar Wind Five*, **CP-2280**, NASA/JPL, Pasadena, 731.

Gosling, J.T., Szabo, A.: 2008, Bifurcated current sheets produced by magnetic reconnection in the solar wind. *J. Geophys. Res.* **113**, A10103. DOI.

Grechnev, V.V., Afanasyev, A.N., Uralov, A.M., Chertok, I.M., Eselevich, M.V., Eselevich, V.G., Rudenko, G.V., Kubo, Y.: 2011, Coronal shock waves, EUV waves, and their relation to CMEs. III. Shock-associated CME/EUV wave in an event with a two-component EUV transient. *Solar Phys.* **273**, 461. DOI.

Harrison, R.A., Davies, J.A., Möstl, C., Liu, Y., Temmer, M., Bisi, M.M., *et al.*: 2012, An analysis of the origin and propagation of the multiple coronal mass ejections of 2010 August 1. *Astrophys. J.* **750**, 45.

Howard, T.A., DeForest, C.E.: 2012a, Inner heliospheric flux rope evolution via imaging of coronal mass ejections. *Astrophys. J.* **746**, 64.

Howard, T.A., DeForest, C.E.: 2012b, The Thomson surface. I. Reality and myth. *Astrophys. J.* **52**, 130.

Howard, T.A., Nandy, D., Koepke, A.C.: 2008, Kinematic properties of solar coronal mass ejections: correction for projection effects in spacecraft coronagraph measurements. *J. Geophys. Res.* **113**, A01104.
Howard, T.A., Tappin, S.J.: 2010, The application of a new phenomenological coronal mass ejection model to space weather forecasting. *Space Weather* **8**, S07004.
Howard, T.A., Fry, C.D., Johnston, J.C., Webb, D.F.: 2007, On the evolution of coronal mass ejections in the interplanetary medium. *Astrophys. J.* **667**, 610.
Howard, R.A., Moses, J.D., Vourlidas, A., Newmark, J.S., Socker, D.G., Plunkett, S.P., *et al.*: 2008, Sun Earth connection coronal and heliospheric investigation (SECCHI). *Space Sci. Rev.* **136**, 67.
Howard, T.A., Howard, T.A., Bisi, M.M., Buffington, A., Clover, J.M., Cooke, M.P., Eyles, C.J., Hick, P.P., Holladay, P.E., Jackson, B.V., Johnston, J.C., *et al.*: 2013, The solar mass ejection imager and its heliospheric imaging legacy. *Space Sci. Rev.* **180**, 1.
Hu, Q., Sonnerup, B.U.Ö.: 2002, Reconstruction of magnetic clouds in the solar wind: orientations and configurations. *J. Geophys. Res.* **107**, A7.
Hu, Q., Smith, C.W., Ness, N.F., Skoug, R.M.: 2004, Multiple flux rope magnetic ejecta in the solar wind. *J. Geophys. Res.* **109**, A03102.
Jackson, B.V.: 2012, The 3D analysis of the heliosphere using interplanetary scintillation and Thomson-scattering observations. In: Bhardwaj, A., Yau, A. (eds.) *Adv. Geosci., Planet. Sci., Terr. Sci.* **30**, 69. DOI.
Jackson, B.V., Buffington, A., Hick, P.P., Altrock, R.C., Figueroa, S., Holladay, P.E., *et al.*: 2004, The solar mass ejection imager (SMEI); the mission. *Solar Phys.* **225**, 177. DOI.
Jackson, B.V., Buffington, A., Hick, P.P., Wang, X., Webb, D.: 2006, Preliminary 3D analysis of the heliospheric response to the 28 October 2003 CME using SMEI white-light observations. *J. Geophys. Res.* **111**, A04S91. DOI.
Jackson, B.V., Buffington, A., Hick, P.P., Clover, J.M., Bisi, M.M., Webb, D.F.: 2010a, The 26 April 2008 CME: SMEI 3-D reconstruction of an ICME interacting with a co-rotating solar wind density enhancement. *Astrophys. J.* **724**, 829.
Jackson, B.V., Hick, P.P., Buffington, A., Bisi, M.M., Clover, J.M.: 2010b, Solar mass ejection imager (SMEI) and interplanetary scintillation (IPS) 3D-reconstructions of the inner heliosphere. *Adv. Geosci.* **21**, 339.
Jackson, B.V., Hick, P.P., Buffington, A., Bisi, M.M., Clover, J.M., Tokumaru, M., Kojima, M., Fujiki, K.: 2011, Three-dimensional reconstruction of heliospheric structure using iterative tomography: a review. *J. Atmos. Solar-Terr. Phys.* **73**, 1214. DOI.
Jackson, B.V., Clover, J.M., Hick, P.P., Buffington, A., Bisi, M.M., Tokumaru, M.: 2013, Inclusion of real-time in-situ measurements into the UCSD time-dependent tomography and its use as a forecast algorithm. *Solar Phys.* **285**, 151. DOI.
Jian, L., Russell, C.T., Luhmann, J.G., Skoug, R.M.: 2006, Properties of interplanetary coronal mass ejections at one AU during 1995 – 2004. *Solar Phys.* **239**, 393. DOI.
Kahler, S.W., Webb, D.F.: 2007, V-arc interplanetary coronal mass ejections observed with the solar mass ejection imager. *J. Geophys. Res.* **112**, A09103.
Kaiser, M.L., Kucera, T.A., Davila, J.M., St. Cyr, O.C., Guhathakurta, M., Christian, E.: 2008, The STEREO mission: an introduction. *Space Sci. Rev.* **136**, 5.
Khrabrov, A.V., Sonnerup, B.U.Ö.: 1998, DeHoffmann–Teller analysis. In: Paschmann, G., Daly, P.W. (eds.) *Analysis Methods for Multi-Spacecraft Data*, Int. Space Sci. Inst, Report, Bern, Switzerland, 221.
Krall, J.: 2007, Are all coronal mass ejections hollow flux ropes? *Astrophys. J.* **657**, 559.
Lepping, R.P., Behannon, K.W.: 1980, Magnetic field directional discontinuities: 1. Minimum variance analysis errors. *J. Geophys. Res.* **85**, 4695.
Lepping, R.P., Jones, J.A., Burlaga, L.F.: 1990, Magnetic field structure of interplanetary magnetic clouds at 1 AU. *J. Geophys. Res.* **95**, 11957.
Lugaz, N., Manchester, W.B. IV, Gombosi, T.I.: 2005, Numerical simulation of the interaction of two coronal mass ejections from Sun to Earth. *Astrophys. J.* **634**, 651.
Lugaz, N., Vourlidas, A., Roussev, I.I.: 2009, Deriving the radial distances of wide coronal mass ejections from elongation measurements in the heliosphere—application to CME-CME interaction. *Ann. Geophys.* **27**, 3479.
Luhmann, J.G., Curtis, D.W., Schroeder, P., McCaulay, J., Lin, R.P., Larson, D.E., *et al.*: 2008, STEREO IMPACT investigation goals, measurements, and data products overview. *Space Sci. Rev.* **136**, 117.
Marubashi, K., Lepping, R.P.: 2007, Long-duration magnetic clouds: a comparison of analyses using torus- and cylinder-shaped flux rope models. *Ann. Geophys.* **25**, 2453.
Millward, G., Biesecker, D.A., Pizzo, V.J., de Koning, C.A.: 2013, An operational software tool for the analysis of coronagraph images: determining CME parameters for input into heliospheric models. *Space Weather* **11**, 57. DOI.
Möstl, C., Farrugia, C.J., Miklenic, C., Temmer, M., Galvin, A.B., Luhmann, J.G., Kilpua, E.K.J., Leitner, M., Nieves-Chincilla, T., Veronig, A., Biernat, H.K.: 2009, Multi-spacecraft recovery of a magnetic cloud and its origin from magnetic reconnection on the Sun. *J. Geophys. Res.* **114**, A04102. DOI.

Muhr, N., Veronig, A.M., Kienreich, I.W., Temmer, M., Vrsnak, B.: 2011, Analysis of characteristic parameters of large-scale coronal waves observed by the solar-terrestrial relations observatory/extreme ultraviolet imager. *Astrophys. J.* **739**, 8.

Pizzo, V.J., Biesecker, D.A.: 2004, Geometric localization of STEREO CMEs. *Geophys. Res. Lett.* **31**, L21802. DOI.

Qiu, J., Hu, Q., Howard, T.A., Yurchyshyn, V.B.: 2007, On the magnetic flux budget in low-corona magnetic reconnection and interplanetary coronal mass ejections. *Astrophys. J.* **695**, 758.

Riley, P., Linker, J.A., Lionello, R., Mikic, Z., Odstrcil, D., Hidalgo, M.A., Cid, C., Hu, Q., Lepping, R.P., Lynch, B.J., Rees, A.: 2004, Fitting flux ropes to a global MHD solution: a comparison of techniques. *J. Atmos. Solar-Terr. Phys.* **66**, 1321.

Rouillard, A.P., Davies, J.A., Forsyth, R.J., Rees, A., Davis, C.J., Harrison, R.A., *et al.*: 2008, Bifurcated current sheets produced by magnetic reconnection in the solar wind. *Geophys. Res. Lett.* **35**, L10110. DOI.

Sauvaud, J.-A., Larson, D., Aoustin, C., Curtis, D., Médale, J.-L., Fedorov, A., *et al.*: 2008, The IMPACT solar wind analyzer (SWEA). *Space Sci. Rev.* **136**, 227.

Sheeley, N.R. Jr., Walters, J.H., Wang, Y.M., Howard, R.A.: 1999, Continuous tracking of coronal outflows: two kinds of coronal mass ejections. *J. Geophys. Res.* **104**, 24739.

Sheeley, N.R. Jr., Herbst, A.D., Palatchi, C.A., Wang, Y.-M., Howard, R.A., Moses, J.D., *et al.*: 2008, Heliospheric images of the solar wind at Earth. *Astrophys. J.* **675**, 853.

Sonnerup, B.U.Ö., Cahill, L.J.: 1967, Magnetopause structure and attitude from Explorer observations. *J. Geophys. Res.* **72**, 171.

Stenborg, G., Cobelli, P.J.: 2003, A wavelet packets equalization technique to reveal the multiple spatial-scale nature of coronal structures. *Astron. Astrophys.* **398**, 1185.

Tappin, S.J., Howard, T.A.: 2009, Direct observation of a corotating interaction region by three spacecraft. *Astrophys. J.* **702**, 862. DOI.

Temmer, M., Vrsnak, B., Veronig, A.M.: 2013, The wave-driver system of the off-disk coronal wave of 17 January 2010. *Solar Phys.* **287**, 441. DOI.

Thernisien, A., Vourlidas, A., Howard, R.A.: 2009, Forward modeling of coronal mass ejections using STEREO/SECCHI data. *Solar Phys.* **256**, 111. DOI.

Tóth, G., van der Holst, B., Sokolov, I.V., De Zeeuw, D.L., Gombosi, T.I., Fang, F., *et al.*: 2012, Adaptive numerical algorithms in space weather modeling. *J. Comput. Phys.* **231**, 870.

Vandas, M., Romashets, E.P.: 2003, Force-free field with constant alpha in an oblate cylinder: a generalization of the Lundquist solution. *Astron. Astrophys.* **398**, 801.

Vandas, M., Romashets, E., Geranios, A.: 2010, How do fits of simulated magnetic clouds correspond to their real shapes in 3D? *Ann. Geophys.* **28**, 1581.

Vandas, M., Romashets, E., Watari, S.: 2005, Magnetic clouds of oblate shapes. *Planet. Space Sci.* **53**(1), 19.

Veronig, A.M., Muhr, N., Kienreich, J.W., Temmer, M., Vrsnak, B.: 2010, First observations of a dome-shaped large-scale coronal extreme-ultraviolet wave. *Astrophys. J. Lett.* **716**, L57.

Vourlidas, A., Howard, R.A., Esfandiari, E., Patsourakos, S., Yashiro, S., Michalek, G.: 2010, Comprehensive analysis of coronal mass ejection mass and energy properties over a full solar cycle. *Astrophys. J.* **722**, 1522. DOI.

Vourlidas, A., Lynch, B.J., Howard, R.A., Li, Y.: 2013, How many CMEs have flux ropes? Deciphering the signatures of shocks, flux ropes, and prominences in coronagraph observations of CMEs. *Solar Phys.* **284**, 179. DOI.

Webb, D.F., Mizuno, D.R., Buffington, A., Cooke, M.P., Eyles, C.J., Fry, C.D., *et al.*: 2006, Solar mass ejection imager (SMEI) observations of CMEs in the heliosphere. *J. Geophys. Res.* **111**, A12101. DOI.

Webb, D.F., Möstl, C., Jackson, B.V., Bisi, M.M., Howard, T.A., Mulligan, T., *et al.*: 2012, Heliospheric imaging of 3D density structures during the multiple coronal mass ejections of late July to early August 2010. *Solar Phys.* **285**, 317.

Wood, B.E., Howard, R.A.: 2009, An empirical reconstruction of the 2008 April 26 coronal mass ejection. *Astrophys. J.* **702**, 901.

Wood, B.E., Howard, R.A., Socker, D.G.: 2010, Reconstructing the morphology of an evolving coronal mass ejection. *Astrophys. J.* **715**, 1524.

Wood, B.E., Karovska, M., Chen, J., Brueckner, G.E., Cook, J.W., Howard, R.A.: 1999, Comparison of two coronal mass ejections observed by EIT and LASCO with a model of an erupting magnetic flux rope. *Astrophys. J.* **512**, 484.

Wood, B.E., Howard, R.A., Thernisien, A., Plunkett, S.P., Socker, D.G.: 2009, Reconstructing the 3D morphology of the 17 May 2008 CME. *Solar Phys.* **259**, 163.

Wood, B.E., Wu, C.-C., Howard, R.A., Socker, D.G., Rouillard, A.P.: 2011, Empirical reconstruction and numerical modeling of the first geoeffective coronal mass ejection of solar cycle 24. *Astrophys. J.* **729**, 70.

Zhao, X.H., Wu, S.T., Wang, A.H., Vourlidas, A., Feng, X.S., Jiang, C.W.: 2011, Uncovering the wave nature of the EIT wave for the 2010 January 17 event through its correlation to the background magnetosonic speed. *Astrophys. J.* **742**, 131.

Zuccarello, F.P., Bemporad, A., Jacobs, C., Mierla, M., Poedts, S., Zuccarello, F.: 2012, The role of streamers in the deflection of coronal mass ejections: comparison between STEREO three-dimensional reconstructions and numerical simulations. *Astrophys. J.* **744**, 66.